

Towards High-Fidelity Gaussian Splatting with Queried-Convolution Neural Networks

Abhinav Kumar¹, Tristan Aumentado-Armstrong^{2*}, Lazar Valkov^{1*}
 Gopal Sharma¹, Alex Levinshtein², Radek Grzeszczuk^{1,2}, Suren Kumar¹
¹Samsung Research America, AI Center – Mountain View, CA, USA
²Samsung Research, AI Center – Toronto, ON, Canada
 {a.kumar4, tristan.a, lazar.valkov, gopal.sharma}@samsung.com
 {alex.lev, radek.g, suren.kumar}@samsung.com

Project Page: <https://abhi1kumar.github.io/qonvolution/>

Abstract. Gaussian Splatting has revolutionized the field of Novel View Synthesis (NVS) with faster training and real-time rendering. However, its reconstruction fidelity still trails behind the powerful radiance models such as Zip-NeRF. Motivated by our theoretical result that both queries (such as coordinates) and neighborhood are important to learn high-fidelity signals, this paper proposes Queried-Convolutions (Qonvolutions), a simple yet powerful modification using the neighborhood properties of convolution. Qonvolutions convolve a low-fidelity signal with queries to output residual and achieve high-fidelity reconstruction. We empirically demonstrate that combining Gaussian splatting with Qonvolution neural networks (QNNs) results in state-of-the-art NVS on real-world scenes, even outperforming Zip-NeRF on image fidelity. QNNs also enhance performance of 1D regression, 2D regression and 2D super-resolution tasks.

Keywords: Gaussian Splatting · Qonvolutions · High-fidelity



Fig. 1: 3DGS with Qonvolution. Adding Qonvolution Neural Network (QNN) faithfully reconstructs details and results in higher fidelity synthesis than 3D Gaussian Splatting [38]. We highlight the differences in inset figures.

1 Introduction

Novel View Synthesis (NVS) aims to render a scene from an unseen viewpoint, based on a finite set of input images and their associated camera poses. This task is a cornerstone of modern computer graphics, with applications ranging from dynamic scene reconstruction [24] to 3D content creation [79, 98, 103].

* Equal Second Authors.

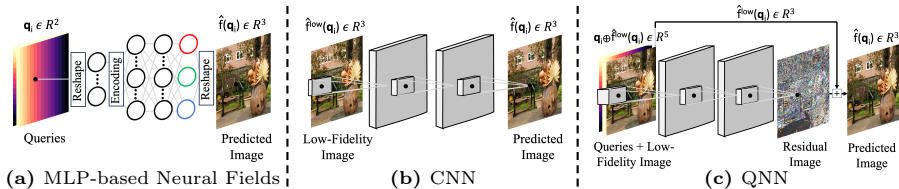


Fig. 2: Overview of MLPs, CNNs and QNNs. MLPs take (encoded) queries $\gamma(\mathbf{q}_i)$ and uses linear layers. CNNs take the low-fidelity signal \hat{f}^{low} and uses convolutions. QNN concatenates the low-fidelity signal \hat{f}^{low} to the (encoded) queries $\gamma(\mathbf{q}_i)$ and uses convolutions. [Key: Freq = Frequency, \oplus = Concatenation].

This field underwent a paradigm shift with the introduction of Neural Radiance Field (NeRF) [59], and more recently, 3D Gaussian Splatting (3DGS) [38]. While NeRFs pioneered high-quality volumetric rendering [8], 3DGS offers faster training and real-time rendering.

Several extensions of 3DGS have followed that refine initialization [84], exploration [39], primitives [4, 46], multi-scale representations [97], and frequency-weighting [100]. However, its reconstruction fidelity still trails behind the powerful radiance models such as Zip-NeRF [8]. We observe that a bottleneck in achieving high-fidelity (HF) 3DGS lies in the sub-optimal color (Spherical Harmonics) parameters within 3D gaussians (Fig. 8) and difficulty in representing the fine structural details.

The challenge of capturing details in neural networks has spurred a rich and diverse body of research within two classes of tasks. One stream, which includes the popular novel view synthesis (NVS) task with NeRFs, uses Multi-Layer Perceptrons (MLPs) (Fig. 2a) to directly fit signals. Key strategies within this stream include modifying positional encodings [77], altering activations [73], and predicting Fourier series coefficients [44]. However, MLPs lack the necessary inductive biases [21, 42] to capture the local neighborhood dependencies inherent in most 1D and 2D signals. We conjecture that these local relationships are crucial for learning details effectively. By processing data points or pixels in isolation, existing MLPs often neglect these local connections, which limits their capacity to fully represent HF signals.

Conversely, tasks like 2D super-resolution employ Convolutional Neural Networks (CNNs) to leverage neighborhood information *i.e.* the low-fidelity (LF) signal is convolved with a CNN (Fig. 2b). However, these approaches [35] often do not utilize the information present in the input queries (*e.g.*: spatial coordinates) in predicting the High Fidelity (HF) signal. As shown in previous work [49], architectures that are aware of locality, such as CNNs, often fail at tasks that require even a simple transformations of coordinates. Thus, the potential for queries to also contribute to the reconstruction of details in such tasks remains an area for further investigation.

To address the limitations of existing methods and effectively leverage neighborhood dependencies, valuable queries and LF signals (Theorem 1), this paper introduces Queried-Convolution, or Qconvolution. As a building block, it replaces the traditional linear layer of MLPs with a convolutional layer and processes

queries alongside a LF signal. This approach, which convolves a LF signal with queries to output the residual, marks a departure from MLP-based neural fields and CNNs (see Fig. 2). We empirically demonstrate that combining Gaussian splatting with Qonvolution Neural Networks (QNNs) (Fig. 2c) learns better details (Fig. 1) and even surpasses Zip-NeRF [8] in the 3D NVS task. We additionally show that QNNs¹ benefit 1D regression (Fig. 6), 2D regression, and 2D SR tasks.

In summary, this paper makes the following contributions:

- We propose QNNs, an architecture that convolves both low-fidelity signals and queries to improve the learning of details.
- We theoretically investigate the predictive power of QNNs compared to CNNs (Theorem 1) and the number of Gaussians for increasing fidelity (Corollary 1).
- We empirically show that GS-based baseline with a QNN surpasses Zip-NeRF [8] in the 3D NVS task (Sec. 5.1).
- Our experiments also show that QNNs enhance performance on 1D regression, 2D regression, and 2D SR tasks (Sec. 5.4).

2 Literature Review

Novel-View Synthesis (NVS). Neural Radiance Fields (NeRFs) represent a 3D scene as a continuous function for NVS; however, their reliance on ray-marching results in slow training and rendering [7, 59]. Subsequent research addresses these limitations by introducing better encodings [61, 77] and multi-scale representations [8]. In contrast, 3DGS renders a scene with rasterized 3D gaussians, offering faster training and real-time rendering. Subsequent works improve reconstruction fidelity through better initialization [84], exploration [39], primitives [4, 46], multi-scale representations [97], better projections [31] and frequency-weighting [100]. A few works integrate ray-marching with GS [51], though this typically sacrifices the speed gains. Other studies attempt to generalize NeRFs or GS to multiple scenes [17, 71] or improve efficiency [5] with CNNs. Conversely, this work applies QNNs to rasterized GS images to achieve superior view synthesis. Finally, video diffusion models like CAT3D [24] and LVSM [34] synthesize novel views by concatenating image latents and 3D queries. In contrast, QNN focuses on established NVS benchmarks, rather than sparse-view or generative modelling. Although PRoPE [47] and MVGD [26] concatenate images and queries, they neither use convolutional architectures, nor show that concatenation helps learning HF signal. PaDIS [30] concatenates image coordinates to image as input to a diffusion model.

High-fidelity Learning. MLPs favor learning LF components in a HF signal [65], which poses a significant hurdle in representing complex signals. A closely related phenomenon is the low-rank bias [33]. To combat these limitations, the literature presents a variety of strategies. The first prominent direc-

¹ Except for SR, this paper mostly covers coordinate-based networks (neural fields) for regression, where the focus is fitting to a single signal than in generalizable or amortized models.

tion involves modifying positional encodings. Techniques like sinusoidal encodings [83], Fourier encodings [66,77] and hash-grids [61] provide MLPs with more discriminative spatial information, which helps them learn higher frequencies. Similarly, [96] feeds wavelet-decomposed signals into neural networks, leveraging the multi-resolution properties of wavelets. Another direction centers on redesigning activation functions to boost the MLP capacity for HF representation. Examples include the use of the error function (erf) [94], the periodic activations in SIREN [73], sinc functions [69], FINER [50] or QIREN functions [102]. Some methods also work directly in the frequency domain, either by predicting Fourier series coefficients [44] or phase-shifted signals [14]. High-frequency weighted losses [70,100] is another effective strategy, that reconstructs fine-grained details during training. Additional efforts to overcome include carefully tuning weight initialization [69,80] for more balanced learning across all frequencies. Some methods employ network ensembles [3,87] to collectively capture this information. Compared to these prior methods, which primarily use MLPs over queries, this paper convolves both queries and the LF signal. This leverages neighborhood and the LF signal for superior signal learning.

Image Super-Resolution (SR). The SR literature is seeing a paradigm shift from Generative Adversarial Networks (GANs) [85] to diffusion models [68,99], primarily building on CNNs [85], with some exceptions [43]. To achieve arbitrary resolution, implicit representations are a key strategy [18,43]. In this context, QNN stands apart by integrating queries and encoded images through convolutions, contrasting with MLP-based processing of queries and latents. While [43] also use CNNs and queries, their core innovation centers on predicting Fourier space coefficients in the output, whereas QNN focuses on the convolutional mechanism for query integration.

Theoretical Results. Many theoretical works demonstrate that CNNs exhibit superior sample complexity compared to MLPs, for both binary classification [9,48] and regression problems [22,60,90], provided certain conditions are met. Many common computer vision tasks, including NVS, meet these conditions [82]. Some attribute the enduring utility of the CNN to its inductive biases, specifically weight sharing [11,45,57] and neighborhood [41,55,64]. For example, [55] showed that CNNs learn more accurate mappings than MLPs when the classification label depends on the neighborhood information. To the best of our knowledge, no theoretical results directly compare QNNs with CNNs and MLPs in regression settings.

3 Background

We begin by establishing the basics in the following paragraphs.

3D Gaussian Splatting. The 3DGS [38] represents a scene with a collection of learnable 3D gaussian primitives $\mathcal{G} = \{G_k\}_{k=1}^K$, each parametrized by opacity, location, rotation, scale, and color (represented by spherical harmonics or SH). The opacity $\alpha_k \in [0, 1]$ of Gaussian G_k at spatial point $x \in \mathbb{R}^3$ is given by $\sigma_k(x) = \alpha_k \exp\left(-\frac{1}{2}(x - \mu_k)^\top \Sigma_k^{-1}(x - \mu_k)\right)$ where $\Sigma_k = R_k S_k S_k^\top R_k^\top \in \mathbb{R}^{3 \times 3}$ is

the covariance matrix controlling the ellipsoid’s spatial distribution. 3DGS employs rasterization for color rendering. With K_r Gaussians intersecting the ray r , which are ordered by ascending depth d_k^r , the rendering equations are

$$c(r) = \sum_{k=1}^{K_r} c_k \sigma(x_k^r) \tau_k, \quad d(r) = \sum_{k=1}^{K_r} d_k^r \sigma(x_k^r) \tau_k \quad (1)$$

where $\tau_k = \prod_{j=1}^{k-1} (1 - \sigma(x_j^r))$ and c and d denote the rendered color and depth values of the 3D Gaussian scene \mathcal{G} along ray r . See [38] for more details.

Neural Fields. A neural field, denoted as $\hat{f}_\theta : \mathcal{Q} \rightarrow \mathcal{O}$, with parameters θ , represents a signal by mapping a bounded set of queries $\mathcal{Q} \subset \mathbb{R}^d$ to outputs $\mathcal{O} \in \mathbb{R}^m$. Specifically, for an input query vector $\mathbf{q}_i \in \mathcal{Q}$, the neural field produces an output $\hat{f}_\theta(\mathbf{q}_i) \in \mathcal{O}$. This framework is highly versatile, accommodating diverse signal types and queries, such as 1D audio, 2D images, or 3D geometry. Illustrative examples of tasks, inputs and their corresponding outputs include:

- 1D Regression: 1D coordinate queries $\mathbf{q}_i \in \mathbb{R}^1$, outputting 1D scalar values [77];
- 2D Image Regression: 2D coordinate queries $\mathbf{q}_i \in \mathbb{R}^2$, representing pixel locations, outputting 3D RGB pixel colors [74];
- NVS with NeRF: 5D queries² $\mathbf{q}_i \in \mathbb{R}^5$, combining 3D camera coordinates with 2D view directions, outputting 4D color and density information [59].

Most neural fields commonly employ MLPs to implement the function \hat{f}_θ . To construct details, they first pass a query \mathbf{q}_i through an encoding γ such as Fourier encodings [77] and hash-grids [61]. So, we write the neural field as

$$\hat{f}_\theta^{MLP}(\mathbf{q}_i) = MLP(\gamma(\mathbf{q}_i)). \quad (2)$$

Vanilla encoding refers to $\gamma(\mathbf{q}_i) = \mathbf{q}_i$. The neural field processes N input samples \mathbf{q}_i , each with $d=C_{in}$ input dimensions (channels), C_h hidden dimensions (channels) and generates N output samples with $m=C_{out}$ output dimensions (channels). Consequently, the neural field transforms a tensor of shape $N \times C_{in}$ into an output tensor of shape $N \times C_{out}$. One then reshapes the output samples to match the target signal dimensions. One optimizes the parameters θ of these networks by minimizing a loss, such as the squared or the \mathcal{L}_1 loss between the network’s output and the true signal, over the observed data.

Example. As an example, consider a 2D image regression task where 2D coordinates serve as queries. In this scenario, the input channels C_{in} are 2, representing the (u, v) pixel coordinates, and the output channels C_{out} are 3, corresponding to the RGB pixel colors. For each image, the number of data samples, i , ranges from 1 to N , where $N=H \times W$ (height times width of the image).

4 Queried-Convolution Neural Networks (QNN)

Having established the necessary notations and preliminaries in the preceding section, we now introduce our proposed Qonvolution and QNN in this section.

² In practice, NeRF uses 6D queries with 3D view directions of norm 1.

4.1 QNN

Let \hat{f}^{low} and f^{low} respectively be the predicted (learned) and the true LF approximation of the ground truth (GT) signal f . Note that this LF signal is often available in certain tasks: for example, the NVS task can use the splatted 3DGS image as the learned LF signal, while the SR task itself provides a GT low-pass image as the input.

We hypothesize that there is benefit to providing the LF approximation of neighboring coordinates. So, we set out to design a neural field which exploits the information present in the neighborhood of the given query \mathbf{q} in terms of the query values and the corresponding LF approximations. Then, the Qconvolution neural network (QNN) concatenates the neighborhood of encoded input queries $\gamma(\mathbf{q}_{\mathcal{N}(i)})$ with their LF signal $\hat{f}_{\mathcal{N}(i)}^{low}$, and subsequently convolves them to produce the output $\hat{f}_{\theta}(\mathbf{q}_i) \in \mathcal{O}$, with $\mathcal{N}(i)$ denoting the neighbors of index i including itself. We formally write the QNN as

$$\hat{f}_{\theta}^{QNN}(\mathbf{q}_i) = CNN(\gamma(\mathbf{q}_{\mathcal{N}(i)}) \oplus \hat{f}_{\mathcal{N}(i)}^{low}), \quad (3)$$

with \oplus denoting the concatenation of tensors along the channel dimensions. With LF signal f^{low} available, we ask the QNN to learn the residual, and so the final output $\hat{f}_{\theta}(\mathbf{q}_i)$ adds the LF and the residual as

$$\hat{f}_{\theta}(\mathbf{q}_i) = \hat{f}^{low}(\mathbf{q}_i) + CNN(\gamma(\mathbf{q}_{\mathcal{N}(i)}) \oplus \hat{f}_{\mathcal{N}(i)}^{low}), \quad (4)$$

A distinct advantage of the QNN architecture is that it needs to be evaluated once for the entire signal, rather than once per coordinate. However, a downside is QNNs can not be used in tasks without neighborhoods such as casting a single ray in NeRF. Furthermore, the QNN architecture offers considerable flexibility in the choice and integration of queries; various queries can be appended depending on the specific task at hand. We refer to our ablation studies (Sec. 5.3), where we experiment with different queries.

Example. To illustrate, consider the same 2D image regression task previously discussed in Sec. 3, characterized by $C_{in}=2$ input channels and $C_{out}=3$ output channels. The number of data samples for each image is $N=H \times W$. In this context, the LF image is a tensor of shape $C_{low} \times H \times W$. The QNN appends both this LF tensor and the 2D coordinate queries. Consequently, the QNN receives an input tensor of shape $(C_{low} + C_{in}) \times H \times W$, or $5 \times H \times W$, and outputs a $C_{out} \times H \times W$, or $3 \times H \times W$ tensor without reshaping.

Remarks. The QNN generalizes several existing architectures in the literature:

- Replacing the CNN with an MLP and excluding the LF signal \hat{f}^{low} , reduces the QNN to conventional neural fields.
- By omitting the input queries \mathbf{q}_i , the QNN effectively simplifies to a standard CNN architecture.
- When utilizing normalized 2D coordinates as queries with vanilla encodings and employing 2D convolutions, QNN becomes the coordinate CNN [49].

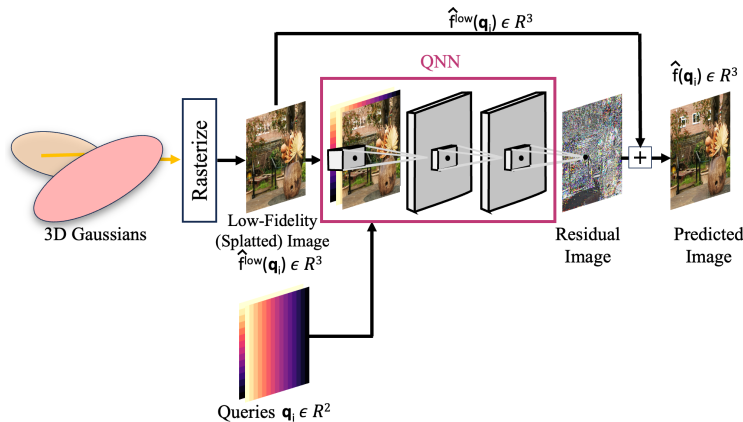


Fig. 3: GS+QNN Architecture. QNN takes the 2D LF splatted image and queries as input to output the residual image, which is then added to the splatted image to get the final predicted novel view image.

4.2 Comparing QNN, CNN and MLP on Regression Tasks

In this subsection, we provide theoretical justification for our approach with real-valued target functions. We show that, in the setting which is not limited by data nor computation, adding contextual information, specifically neighborhood information and then the neighboring queries, does not negatively impact the achievable risk when predicting from a LF signal. Furthermore, we show that, in this setting, adding queries guarantees to perfectly approximate the target function, achieving the best possible error. See Sec. B.1 for the proof.

Theorem 1. *Let \mathcal{X} be an input space, which is a discrete integer lattice or in \mathbb{R}^d , and let $P_{\mathcal{X}}$ be a probability distribution on \mathcal{X} . Let $f: \mathcal{X} \rightarrow [0, 1]$ be a deterministic and measurable target function. A feature map is a deterministic, measurable function $\phi: \mathcal{X} \rightarrow \mathcal{Z}$ that maps inputs to a feature space \mathcal{Z} . The corresponding hypothesis class, $\mathcal{H}(\phi)$, is the set of all deterministic, measurable functions mapping from \mathcal{Z} to the output space $[0, 1]$. The optimal expected error for a given feature map ϕ is the minimum mean squared error achievable by any hypothesis in its class $\mathcal{R}^*(\phi, f) = \min_{h \in \mathcal{H}(\phi)} \mathbb{E} [(f(x) - h(\phi(x)))^2]$. Let $f^{low}: \mathcal{X} \rightarrow [0, 1]$ be a deterministic measurable function that approximates f . Consider the sequence of increasingly informative feature maps:*

- **Feature Map 1 (Approximation) or MLP (LF):** $\phi_1(x) = (f^{low}(x))$
- **Feature Map 2 (Neighborhood) or CNN (LF):** $\phi_2(x) = (\phi_1(x - \Delta), \phi_1(x), \phi_1(x + \Delta))$
- **Feature Map 3 (Neighborhood and Queries) or QNN:** $\phi_3(x) = (\phi_2(x), x, x - \Delta, x + \Delta)$,

for a fixed $\Delta > 0$. Then, the optimal expected errors for these feature maps are monotonically non-increasing and bounded by zero:

$$\mathcal{R}^*(\phi_1, f) \geq \mathcal{R}^*(\phi_2, f) \geq \mathcal{R}^*(\phi_3, f) = 0 \quad (5)$$

Table 1: Experimental Settings for tasks. We add the predicted/GT LF signal to the network’s residual output \hat{f} to get the final prediction $\hat{f}^{low} + \hat{f}(\mathbf{q}, \hat{f}^{low})$. The loss is computed between the final prediction $\hat{f}^{low} + \hat{f}(\mathbf{q}, \hat{f}^{low})$ and the GT signal f . [Key: Conv= Convolution, Pred= Predicted, Out= Output].

Task	Dimensionality (Channels)				LF Input (f^{low} / \hat{f}^{low})	Network Output	Final Output	Network (\hat{f})	Loss
	Query $q(d)$	LF(C_{low})	Conv	Out (m)					
3D NVS	2	3	2D	3				QNN, MLP, CNN	\mathcal{L}_1 variant
2D Reg	2	3	2D	3	Pred \hat{f}^{low}	$\hat{f}(\mathbf{q}, \hat{f}^{low})$	$\hat{f}^{low} + \hat{f}(\mathbf{q}, \hat{f}^{low})$	QNN, MLP	\mathcal{L}_1
1D Reg	1	1	1D	1				QNN, MLP, CNN	
2D SR	2	3	2D	3	GT f^{low}	$\hat{f}(\mathbf{q}, f^{low})$	$f^{low} + \hat{f}(\mathbf{q}, f^{low})$	QNN, CNN	\mathcal{L}_1

4.3 Combining Gaussian Splatting with QNN

Fig. 3 shows the architecture of combining Gaussian Splatting (GS) with QNN to enhance image fidelity. We integrate QNN into GS as follows³. The GS renders the initial LF signal \hat{f}^{low} . The QNN concatenates the query \mathbf{q} and the LF splatted image \hat{f}^{low} as input. The QNN passes the concatenation through a CNN to produce a residual image $QNN(\mathbf{q}, \hat{f}^{low})$. We then add the LF splatted image \hat{f}^{low} and this residual image to produce the final predicted novel view image $\hat{f}_\theta^{GS+QNN} = \hat{f}^{low} + QNN(\mathbf{q}, \hat{f}^{low})$. We compare the prediction from the GS+QNN model \hat{f}_θ^{GS+QNN} against the GT image f with the same loss as the corresponding baseline. More details are in Sec. C.1.

Note. Unlike ray marching methods (NeRF) which require multiple queries per pixel, QNN requires exactly one query per pixel, significantly speeding up the process without increasing training time. We confirm this empirically in Sec. 5.1.

Shortcoming of Gaussian-based Representation. Our next Corollary 1 states that increasing fidelity (PSNR) or decreasing MSE for gaussian-based representation requires increasing the number of gaussians exponentially. We defer its proof to Sec. B.2, and confirm this empirically in Sec. 5.2.

Corollary 1 (of Theorem 2 in Supp, #Gaussians). *Let a 2D image be a measurable real-valued function whose first derivative exists at all points. Then, the minimum number of 2D splatted gaussians, n , required to achieve an approximation MSE of ϵ is bounded below by $n \geq \exp \left[W \left(\frac{\epsilon}{c} \right)^2 \right]$, where W denotes the Lambert W function and c is a constant independent of ϵ .*

5 Experiments

We evaluate on four tasks including 3D NVS, 1D and 2D regression, and 2D SR. Tab. 1 summarizes all these tasks. The NVS, 1D and 2D regression experiments compares QNNs against MLP-based neural fields and CNNs, while 2D SR experiments compares QNNs against CNNs.

5.1 3D NVS

Datasets. Our NVS experiments use six datasets: Mip-NeRF 360 [7], Tank & Temples [40], Deep Blending [28], OMMO [52], Shelly [89] and Syn-NeRF [59].

³ We drop the independent variable x and subscript i in query \mathbf{q}_i for brevity.

Table 2: NVS Results. Adding QNN outperforms the baselines across all datasets. Numbers are from respective papers. Stable-GS, 3D-HGS and MCMC do not report results on all nine scenes of Mip-NeRF 360 dataset. Zip-NeRF Syn-NeRF numbers are from their official repository. Scenewise details in Tab. 17. [Key: **Best**, **Second-best**, **Third-best**, [♠]= Reported, * = Retrained, † = Reported in 3DGS [38]].

	Method	Mip-NeRF 360[7]			Tank & Temples[40]			Deep Blending[28]			OMMO [52]			Shelly [89]			Syn-NeRF [59]		
		PSNR ↑ / SSIM ↑ / LPIPS ↓	PSNR ↑ / SSIM ↑ / LPIPS ↓	PSNR ↑ / SSIM ↑ / LPIPS ↓	PSNR ↑ / SSIM ↑ / LPIPS ↓	PSNR ↑ / SSIM ↑ / LPIPS ↓	PSNR ↑ / SSIM ↑ / LPIPS ↓	PSNR ↑ / SSIM ↑ / LPIPS ↓	PSNR ↑ / SSIM ↑ / LPIPS ↓	PSNR ↑ / SSIM ↑ / LPIPS ↓	PSNR ↑ / SSIM ↑ / LPIPS ↓	PSNR ↑ / SSIM ↑ / LPIPS ↓	PSNR ↑ / SSIM ↑ / LPIPS ↓	PSNR ↑ / SSIM ↑ / LPIPS ↓	PSNR ↑ / SSIM ↑ / LPIPS ↓	PSNR ↑ / SSIM ↑ / LPIPS ↓	PSNR ↑ / SSIM ↑ / LPIPS ↓	PSNR ↑ / SSIM ↑ / LPIPS ↓	
Ray	Plenoxels [†] [37]	CVPR22	23.08 / 0.63 / 0.44	21.08 / 0.72 / 0.38	23.06 / 0.80 / 0.51	-	-	-	-	-	-	-	-	-	-	-	31.76 / - / -	-	-
	INGP-Big [†] [61]	SIGG22	25.59 / 0.75 / 0.30	21.92 / 0.75 / 0.31	24.96 / 0.82 / 0.39	-	-	-	-	-	-	-	-	-	-	-	33.18 / - / -	-	-
	Adaptive [89]	SIGG23	-	-	-	-	-	-	-	-	-	36.02 / 0.95 / 0.08	32.51 / 0.96 / 0.05	-	-	-	-	-	-
	QFields [72]	ECCV24	-	-	-	-	-	-	-	-	-	37.29 / 0.95 / 0.07	31.00 / 0.95 / 0.07	-	-	-	-	-	-
	3DGRT [51]	SIGG23	27.20 / 0.82 / 0.25	23.20 / 0.83 / 0.22	29.23 / 0.90 / 0.32	-	-	-	-	-	-	-	-	-	-	-	-	-	-
	3DGUT [92]	CVPR23	27.26 / 0.81 / 0.22	22.90 / 0.84 / 0.17	-	-	-	-	-	-	-	-	-	-	-	-	-	-	-
	VKRayGS [12]	CVPR23	27.27 / 0.82 / 0.22	-	-	-	-	-	-	-	-	-	-	-	-	-	-	-	-
	EVER [53]	ICCV23	27.51 / 0.83 / 0.23	-	-	-	-	-	-	-	-	-	-	-	-	-	-	-	-
	Mip-NeRF [†] [6]	CVPR22	27.69 / 0.79 / 0.24	22.22 / 0.76 / 0.26	29.40 / 0.90 / 0.25	-	-	-	-	-	-	-	-	-	-	-	-	-	-
	3DGEER [32]	A&Kw23	27.76 / 0.82 / 0.21	-	-	-	-	-	-	-	-	-	-	-	-	-	-	-	-
	Zip-NeRF [8]	ICCV23	28.54 / 0.83 / 0.19	-	-	-	-	-	-	-	-	-	-	-	-	-	33.69 / 0.97 / -	-	-
	GES [27]	CVPR24	26.91 / 0.79 / 0.25	23.35 / 0.84 / 0.20	29.68 / 0.90 / 0.25	-	-	-	-	-	-	-	-	-	-	-	-	-	-
	Stable-GS [84]	A&Kw23	-	24.04 / 0.86 / 0.16	29.66 / 0.91 / 0.24	-	-	-	-	-	-	-	-	-	-	-	-	-	-
	Convex [29]	CVPR23	27.29 / 0.80 / 0.21	23.95 / 0.85 / 0.16	29.81 / 0.90 / 0.24	-	-	-	-	-	-	-	-	-	-	-	-	-	-
	Vol3DGS [76]	CVPR23	27.30 / 0.81 / 0.21	23.74 / 0.85 / 0.17	29.72 / 0.91 / 0.25	-	-	-	-	-	-	-	-	-	-	-	-	-	-
	Tex-GS [16]	CVPR23	27.35 / 0.83 / 0.19	24.26 / 0.85 / 0.17	28.33 / 0.89 / 0.36	-	-	-	-	-	-	-	-	-	-	-	33.24 / 0.97 / 0.04	-	-
DARB [4]	A&Kw23	27.45 / 0.81 / 0.21	23.64 / 0.85 / 0.17	29.63 / 0.90 / 0.24	-	-	-	-	-	-	-	-	-	-	-	-	-	-	
3D-HGS [46]	A&Kw23	-	25.08 / 0.84 / 0.14	29.80 / 0.90 / 0.25	-	-	-	-	-	-	-	-	-	-	-	-	-	-	
Raster	Project [31]	ICCV23	27.48 / 0.82 / 0.21	23.43 / - / -	29.51 / - / -	-	-	-	-	-	-	-	-	-	-	-	-	-	
	VDGS [56]	CVU24	27.64 / 0.81 / 0.22	24.02 / 0.85 / 0.18	29.54 / 0.91 / 0.24	-	-	-	-	-	-	-	-	-	-	35.97 / 0.99 / 0.01	-	-	
	Revise [13]	ECCV24	27.70 / 0.82 / 0.22	24.10 / 0.86 / 0.18	29.64 / 0.91 / 0.30	-	-	-	-	-	-	-	-	-	-	-	-	-	
	HyRF [91]	NIPS23	27.78 / 0.82 / 0.21	24.02 / 0.84 / 0.18	30.37 / 0.91 / 0.24	-	-	-	-	-	-	-	-	-	-	-	-	-	
	Mip-Splat [97]	CVPR24	27.79 / 0.83 / 0.20	-	-	-	-	-	-	-	-	-	-	-	-	-	-	-	
	FreGS [100]	CVPR24	27.85 / 0.83 / 0.21	23.96 / 0.85 / 0.18	29.93 / 0.90 / 0.24	-	-	-	-	-	-	-	-	-	-	-	-	-	
	3DGS [‡] [38]	SIGG23	27.20 / 0.82 / 0.21	23.14 / 0.84 / 0.18	29.41 / 0.90 / 0.24	-	-	-	-	-	-	-	-	-	-	33.31 / - / -	-	-	
	3DGS* [38]	SIGG23	27.67 / 0.82 / 0.20	23.52 / 0.84 / 0.18	29.50 / 0.90 / 0.24	29.03 / 0.90 / 0.16	37.56 / 0.96 / 0.08	34.83 / 0.98 / 0.03	-	-	-	-	-	-	-	-	-	-	
	3DGS + QNN	-	27.96 / 0.83 / 0.20	24.11 / 0.85 / 0.17	29.67 / 0.91 / 0.25	29.37 / 0.91 / 0.15	37.99 / 0.96 / 0.07	35.36 / 0.98 / 0.03	-	-	-	-	-	-	-	-	-	-	
	MCMC [♠] [39]	NIPS24	-	24.29 / 0.86 / 0.19	29.67 / 0.89 / 0.32	29.52 / 0.91 / 0.20	-	-	-	-	-	-	-	-	-	33.80 / 0.97 / 0.04	-	-	
MCMC* [39]	NIPS24	28.26 / 0.84 / 0.17	24.53 / 0.87 / 0.13	29.32 / 0.91 / 0.24	30.10 / 0.92 / 0.12	35.14 / 0.94 / 0.09	36.14 / 0.98 / 0.02	-	-	-	-	-	-	-	-	-	-		
MCMC + QNN	-	28.58 / 0.84 / 0.16	24.87 / 0.88 / 0.12	29.76 / 0.91 / 0.23	30.34 / 0.92 / 0.12	35.57 / 0.95 / 0.09	36.58 / 0.98 / 0.02	-	-	-	-	-	-	-	-	-	-		

Evaluation Metrics and Baselines. We use PSNR, SSIM [88] and VGG-16 based normalized Learned Perceptual Image Patch Similarity (LPIPS) [101] metrics [38]. We integrate QNN into two GS-based baselines (Fig. 3): 3DGS [38] and MCMC [39]. See Sec. C.1 for more details.

Results. Tab. 2 shows the NVS results on all six datasets. Tab. 2 confirms that adding a QNN outperforms all the baselines and significantly benefits the challenging NVS task. Notably, a QNN with the MCMC baseline surpasses even Zip-NeRF [8] in this task, a testament to its effectiveness.

Training Times. 3DGS, 3DGS + QNN, MCMC, MCMC + QNN and Zip-NeRF models take 0.67, 0.83, 2.00, 2.86 and 32.00⁴ GPU-hours respectively for training on a Mip-NeRF 360 scene measured with V100 GPUs. Thus, MCMC + QNN obtains Zip-NeRF fidelity with 10× lower training time than Zip-NeRF.

High-fidelity Comparison. Tab. 3 reports PSNR_{Edge} on the edges of the Mip-NeRF 360 images as [23]. We first identify Canny edges [15] with thresholds 0, 100, followed by disk dilation of kernel size 3 [23]. Tab. 3 results show that adding QNN improves the PSNR_{Edge} score for both the 3DGS and MCMC baselines, and thus provides superior edge fidelity than baselines and Zip-NeRF.

Qualitative Results. Fig. 5 shows qualitative results using 3DGS [38] baseline on multiple datasets. Adding QNN to 3DGS reconstructs better details resulting in higher fidelity synthesis visually.

⁴ See Tab. 1 of EVER [53].

Table 3: Mip-NeRF 360 PSNR_{Edge} Evaluation. Adding QNN improves PSNR_{Edge} for both 3DGS and MCMC baselines. **MCMC + QNN outperforms Zip-NeRF in PSNR_{Edge}.** [Key: **Best**].

Method	PSNR (↑)	PSNR _{Edge} (↑)
Zip-NeRF [8]	28.54	26.34
3DGS [39]	27.67	25.76
3DGS + QNN	27.96 (+0.29)	25.89 (+0.13)
MCMC [39]	28.26	26.28
MCMC + QNN	28.58 (+0.32)	26.45 (+0.17)

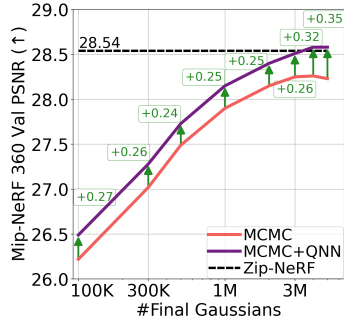


Fig. 4: QNN Scalability. Adding QNN consistently improves MCMC [39] at varied final gaussians.

Table 4: MLP-based Neural Fields with 3DGS [38] baseline on the Mip-NeRF 360 dataset. Adding QNN outperforms all MLPs in fitting training data. We refrain from highlighting if there are more than 5 entries with the same number. [Key: **Best**, **Second-best**, **Third-best**].

Method	Val			Train		
	PSNR (↑)	SSIM (↑)	LPIPS (↓)	PSNR (↑)	SSIM (↑)	LPIPS (↓)
3DGS [38]	27.67	0.82	0.20	29.71	0.90	0.16
3DGS + Vanilla MLP _{same}	27.71	0.83	0.20	29.70	0.89	0.16
3DGS + Vanilla MLP [59]	27.74	0.83	0.20	29.72	0.89	0.16
3DGS + Fourier MLP [77]	27.78	0.82	0.20	29.77	0.89	0.16
3DGS + Hash-grid MLP [61]	27.79	0.82	0.20	29.77	0.89	0.16
3DGS + Erf MLP [94]	27.68	0.82	0.20	29.66	0.89	0.16
3DGS + Sinc MLP [69]	27.68	0.82	0.20	29.66	0.89	0.16
3DGS + SIREN MLP [73]	14.49	0.62	0.51	14.66	0.67	0.49
3DGS + FINER MLP [50]	27.64	0.82	0.20	29.66	0.89	0.16
3DGS + QNN	27.96	0.83	0.20	30.11	0.90	0.16

QNN Scalability. Fig. 4 shows the scalability of QNN with the MCMC baseline [39] on the Mip-NeRF 360 dataset [7] varying the number of final gaussians. It confirms that adding QNN consistently improves NVS at all gaussians.

5.2 Alternatives to QNN

We next consider other alternatives to incorporate details in GS.

MLP-based Neural Fields. We first replace the QNN with several MLP-based neural fields that take queries as inputs. This includes a vanilla MLP (with same or different channels), a Fourier MLP [77], hash-grid MLP [61] and MLPs with Erf [94], Sinc [69], SIREN [73] and FINER [50] activations. None of these alternatives improve NVS performance either on the val or the train sets in Tab. 4. Interestingly, the negligible gain in training PSNR for the Fourier MLP (29.77) vs. 3DGS (29.71) suggests that Fourier MLP **underfits** the training images. In contrast, QNN increases the training performance (30.11), confirming its superior ability to fit the training images.

Adding Parameters to 3D Gaussians. QNN adds parameters in splatted 2D space. An alternative is to add extra 32 parameters to the 3D gaussians in 3D space similar to Textured-GS [16], splatting these parameters, passing through a

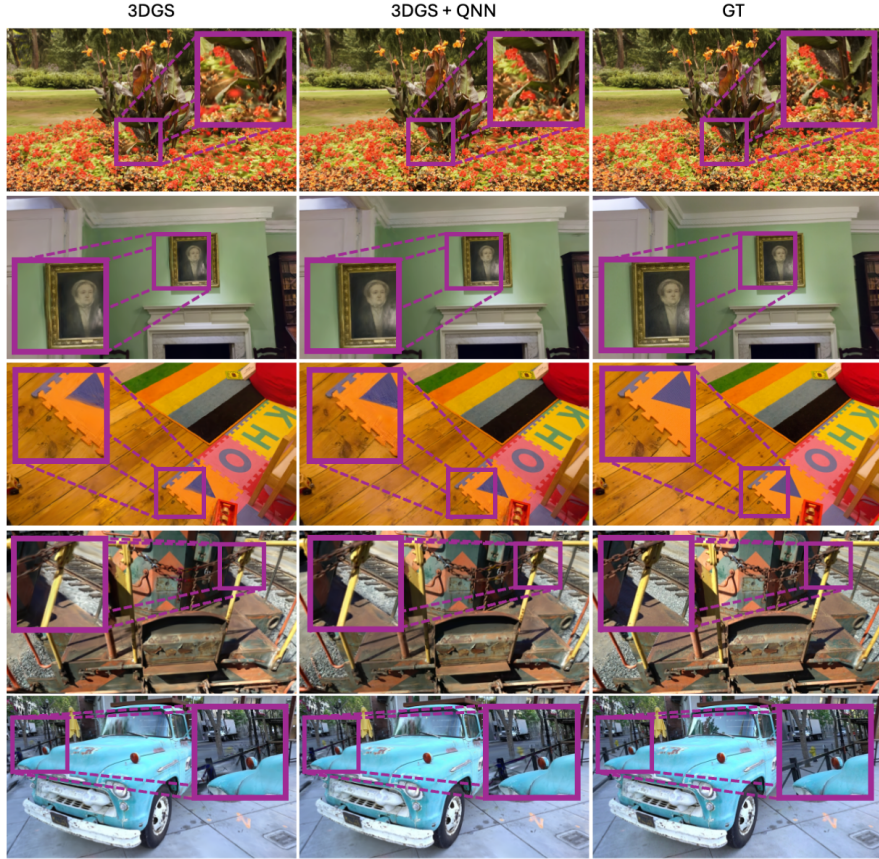


Fig. 5: NVS Qualitative Results. We provide examples of NVS task using 3DGS [38] baseline on multiple datasets. **Adding QNN faithfully reconstructs details** resulting in higher fidelity synthesis visually. Inset figures highlight differences.

Table 5: Adding extra parameters to 3D gaussian of the 3DGS baseline [38] on the Mip-NeRF 360 dataset. Adding parameters to 3D gaussians **overfits on the training data**, and does not generalize well. **QNN shows good generalization (val) and fitting (train) performance.** [Key: Best , Second-best , Third-best].

Method	Val			Train		
	PSNR (▲)	SSIM (▲)	LPIPS (▼)	PSNR (▲)	SSIM (▲)	LPIPS (▼)
3DGS [38]	27.67	0.82	0.20	29.71	0.90	0.16
3DGS + 1-layer CNN	27.47	0.82	0.21	30.12	0.91	0.15
3DGS + 2-layer CNN	26.83	0.81	0.23	30.56	0.92	0.14
3DGS + 4-layer CNN	27.42	0.81	0.23	31.23	0.92	0.14
3DGS + QNN	27.96	0.83	0.20	30.11	0.90	0.16

CNN with varying convolutional layers and then adding as a residual in Tab. 5. Note that this does not change the number of gaussians but only changes the number of parameters per gaussian. Tab. 5 results show that adding parameters to 3D gaussians overfits on the training data and does not generalize well.

Increasing Number of 3D Gaussians. Another potential alternative to improve details is by increasing the number of 3D gaussians. Since the 3DGS base-

Table 6: Increasing number of 3D gaussians of the MCMC baseline [39] on the Mip-NeRF 360 dataset **suffers from optimization difficulties** beyond 4M since the training performance improves but the val performance saturates. Adding QNN **outperforms increasing the gaussians**. [Key: **Best**, **Second-best**, **Third-best**].

Method	#Gaussians (M)	Val			Train		
		PSNR (↑)	SSIM (↑)	LPIPS (↓)	PSNR (↑)	SSIM (↑)	LPIPS (↓)
MCMC [39]	4	28.26	0.84	0.17	30.31	0.91	0.14
MCMC [39]	5	28.23	0.84	0.17	30.51	0.91	0.13
MCMC [39]	6	28.25	0.84	0.17	30.66	0.92	0.13
MCMC [39]	7	28.23	0.84	0.17	30.78	0.92	0.13
MCMC + QNN	4	28.58	0.84	0.16	30.69	0.91	0.14

Table 7: Ablation Studies of QNN with 3DGS [38] on Mip-NeRF 360. QNN performs the best in most metrics. We refrain from highlighting if there are more than 5 entries with the same number. [Key: **Best**, **Second-best**, **Third-best**, \oplus = Concatenation].

Change	From → To	Val			Train		
		PSNR (↑)	SSIM (↑)	LPIPS (↓)	PSNR (↑)	SSIM (↑)	LPIPS (↓)
3DGS [38]	–	27.67	0.82	0.20	29.71	0.90	0.16
Architecture	QNN → Vanilla MLP [59]	27.74	0.83	0.20	29.72	0.89	0.16
	QNN → Fourier MLP [77]	27.78	0.82	0.20	29.77	0.89	0.16
	2D Conv (3×3) → Linear (1×1)	27.83	0.82	0.20	29.84	0.90	0.16
Input	Queries \oplus LF → Queries	27.81	0.82	0.20	29.80	0.90	0.16
	Queries \oplus LF → LF	27.61	0.82	0.20	29.96	0.90	0.16
Queries	2D → 3D location	27.59	0.82	0.19	30.74	0.91	0.14
	2D → 3D location \oplus direction	27.66	0.82	0.20	29.87	0.90	0.16
	2D → Raymap [59]	27.73	0.82	0.20	29.85	0.90	0.16
	2D → Raymap \oplus 2D	27.88	0.82	0.20	30.03	0.90	0.16
	2D → Plücker [1]	27.67	0.82	0.20	29.85	0.90	0.16
Activation	ReLU → Erf [94]	26.43	0.80	0.22	27.98	0.87	0.18
	ReLU → Sinc [69]	27.70	0.82	0.20	29.79	0.90	0.16
	ReLU → FINER [50]	27.33	0.81	0.22	28.62	0.87	0.19
Encoding	Vanilla → Fourier [77]	27.85	0.82	0.20	29.90	0.90	0.16
	Vanilla → Per-axis Fourier	27.85	0.82	0.20	29.89	0.90	0.16
	Vanilla → Exponential [59]	27.94	0.82	0.20	29.99	0.90	0.16
3DGS + QNN	–	27.96	0.83	0.20	30.11	0.90	0.16

line [38] does not restrict the number of 3D gaussians, we go with the MCMC baseline [39] which lets us control the final number of gaussians. Tab. 6 shows that this approach suffers from optimization difficulties beyond 4M gaussians since the training performance improves but the val performance saturates. Fig. 4 also shows this trend where the red curve of MCMC saturates after 3M gaussians. This agrees with Corollary 1 which shows that increasing PSNR needs increasing the number of gaussians exponentially.

5.3 Ablation Studies

To understand the design choices of QNN, we conduct ablations using the 3DGS baseline on the Mip-NeRF 360 dataset [7] following Sec. 5.1. We report metrics on both the val and train sets to evaluate generalization and fitting, respectively.

Architecture. We changed the QNN to vanilla and Fourier MLP [77] as well as 2D convolution to linear layer (3×3→1×1) in QNN. Tab. 7 results reinforces that convolution remains the key for learning details.

Input. We next examined the input to the QNN. Tab. 7 shows that using queries or LF images alone decreases NVS performance on both the val and train sets, confirming input concatenation is crucial for optimal results.

Queries. As explained in Sec. 4, we explored different queries, including:

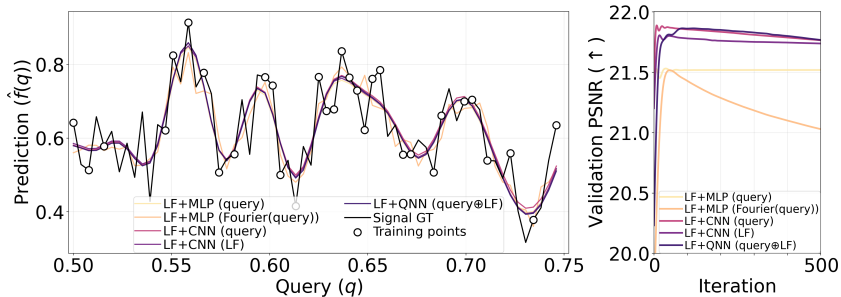


Fig. 6: 1D Regression. This simple experiment compares networks which take the 1D queries and LF signal as input. All networks add LF signal to their residual predictions to produce the final output, which is used in evaluation and training. The standard MLP-based networks including Fourier encodings take 1D coordinates as queries. QNN changes the linear layer to a 1D convolutional layer and also takes the LF signal in addition to the 1D queries. **QNN outperforms MLP-based architectures including Fourier MLPs.** [Key: \oplus = Concatenation].

- 3D location: Unprojecting pixel locations into 3D using camera parameters and splatted depth.
- 3D location \oplus direction: Concatenating 3D view directions to the 3D locations.
- Raymap: Using 3D camera centers with view directions, as in NeRF [59]. [24] refer to this construct as a raymap.
- Raymap \oplus 2D: Appending the 2D queries to the raymap queries.
- Plücker: Using the Plücker rays [1, 25] as queries.

Tab. 7 shows that 2D queries performed best on the validation set, while 3D location queries yielded the best performance on the training set. This divergence warrants further investigation, and we leave a deeper exploration of query performance for future work.

Activation. We then explored changing the ReLU activation within QNN to Erf [94], Sinc [69] and FINER [50] activations. These experiments use our proposed Qonvolution layer, with the only change being the activation. Tab. 7 shows that even these changes prove suboptimal to our best performance.

Encoding. We also change vanilla encodings in QNN with randomized Fourier [77], per-axis Fourier and exponential style NeRF encodings [59]. Changing encodings to any of these decreases performance on both val and train sets.

5.4 Other Tasks

We next evaluate on 1D and 2D regression and SR tasks. Please refer to Tab. 1 for the experimental settings and Sec. C for more details.

1D Regression. We now compare the performance of MLPs, CNNs and our proposed QNNs on a toy 1D regression task. The task involves taking 1D coordinates (and LF signal) as input to produce 1D output. We use the synthetic 1D signal from [77]. Fig. 6 confirms that all CNN models outperform MLPs in PSNR, including Fourier MLP in PSNR.

Table 8: 2D Regression Results. Adding QNN outperforms baselines on this regression task. [Key: **Best**].

Encoding (γ)	QNN	Val		Train	
		PSNR (\uparrow)	SSIM (\uparrow)	PSNR (\uparrow)	SSIM (\uparrow)
Low-frequency images	–	29.61	0.89	29.65	0.89
Hash-grid [61]	×	29.35	0.88	30.34	0.88
Vanilla	×	29.69	0.92	29.69	0.92
	✓	32.48 (+2.79)	0.96 (+0.04)	32.51 (+2.82)	0.96 (+0.04)
Fourier [77]	×	29.79	0.92	29.80	0.92
	✓	32.87 (+3.09)	0.94 (+0.02)	32.93 (+3.13)	0.94 (+0.02)

Table 9: 2D Image SR Results. Adding QNN outperforms baselines across both SR sub-tasks. [Key: **Best**, $\hat{\cdot}$ = Reported, * = Retrained].

Method	QNN	Face SR		Natural SR	
		PSNR (\uparrow)	SSIM (\uparrow)	PSNR (\uparrow)	SSIM (\uparrow)
PULSE [58]	–	16.88	0.44	–	–
FSRGAN [19]	–	23.01	0.62	–	–
SR3 $\hat{\cdot}$ [68]	×	23.04	0.65	–	–
SR3* [68]	×	23.51	0.68	–	–
SR3 [68]	✓	23.63 (+0.12)	0.69 (+0.01)	–	–
Real-ESRGAN $\hat{\cdot}$ [85]	×	–	–	24.84	0.71
Real-ESRGAN* [85]	×	–	–	24.41	0.70
Real-ESRGAN [85]	✓	–	–	24.63 (+0.22)	0.70 (+0.00)

2D Regression. We next evaluate the 2D residual image regression task, where the networks take the 2D coordinates (and LF image) as input to output three-dimensional RGB values. We use the Mip-NeRF 360 dataset [7] for this experiment. Tab. 8 confirms that adding QNN benefits learning details for 2D residual image regression task on both val and train splits.

2D Super-Resolution (SR). We further evaluate on Face and Natural image SR tasks in Tab. 9. The findings confirm that adding QNNs consistently increases the fidelity for both SR sub-tasks. Fig. 7 in Supp shows qualitative results.

6 Conclusions

Gaussian Splatting has revolutionized the field of Novel View Synthesis (NVS) with faster training and real-time rendering. However, its reconstruction fidelity still trails behind the powerful radiance models such as Zip-NeRF. Motivated by our theoretical result that both queries (such as coordinates) and neighborhood are important to learn high-fidelity signals, this paper proposes Queried-Convolutions (Qonvolutions), a simple yet powerful modification using the neighborhood properties of convolution. Qonvolutions convolve a low-fidelity signal with queries to output residual and achieve high-fidelity reconstruction. We empirically demonstrate that combining Gaussian splatting with Qonvolution neural networks (QNNs) results in state-of-the-art NVS on real-world scenes, even outperforming Zip-NeRF on image fidelity. QNNs also enhance performance of 1D regression, 2D regression and 2D super-resolution tasks. Future work involves exploring whether advances in neural implicit fields arising from orthogonal research directions are also beneficial for QNNs.

Limitations. QNNs require neighborhood information for processing. QNNs cannot be used in tasks without neighborhoods such as casting a single ray in a NeRF [59] or in SDF [62].

References

1. Plücker, J.: Analytisch-geometrische Entwicklungen, vol. 1. GD Baedeker (1828) [12](#), [13](#)
2. Agustsson, E., Timofte, R.: NTIRE 2017 challenge on single image super-resolution: Dataset and study. In: CVPR workshops (2017) [30](#), [31](#)
3. Ainsworth, M., Dong, J.: Galerkin neural network approximation of singularly-perturbed elliptic systems. *Computer Methods in Applied Mechanics and Engineering* (2022) [4](#)
4. Arunan, V., Nazar, S., Pramuditha, H., Viruthshaan, V., Ramasinghe, S., Lucey, S., Rodrigo, R.: DARB-Splatting: Generalizing splatting with decaying anisotropic radial basis functions. arXiv preprint arXiv:2501.12369 (2025) [2](#), [3](#), [9](#)
5. Aumentado-Armstrong, T., Mirzaei, A., Brubaker, M., Kelly, J., Levinshtein, A., Derpanis, K., Gilitschenski, I.: Exploring reconstructive latent-space neural radiance fields. In: ICCV Workshops (2023) [3](#)
6. Barron, J., Mildenhall, B., Tancik, M., Hedman, P., Martin-Brualla, R., Srinivasan, P.: Mip-NeRF: A multiscale representation for anti-aliasing neural radiance fields. In: ICCV (2021) [9](#)
7. Barron, J., Mildenhall, B., Verbin, D., Srinivasan, P., Hedman, P.: Mip-NeRF 360: Unbounded anti-aliased neural radiance fields. In: CVPR (2022) [3](#), [8](#), [9](#), [10](#), [12](#), [14](#), [21](#), [27](#), [28](#), [30](#), [31](#), [32](#), [34](#), [35](#), [37](#)
8. Barron, J., Mildenhall, B., Verbin, D., Srinivasan, P., Hedman, P.: Zip-NeRF: Anti-aliased grid-based neural radiance fields. In: ICCV (2023) [2](#), [3](#), [9](#), [10](#), [32](#), [33](#), [35](#), [37](#)
9. Bietti, A.: Approximation and learning with deep convolutional models: a kernel perspective. In: ICLR (2021) [4](#)
10. Bishop, C., Nasrabadi, N.: Pattern recognition and machine learning. Springer (2006) [23](#)
11. Bruna, J., Mallat, S.: Invariant scattering convolution networks. TPAMI (2013) [4](#)
12. Bulò, S., Bartolovic, N., Porzi, L., Kotschieder, P.: Hardware-rasterized ray-based gaussian splatting. In: CVPR (2025) [9](#)
13. Bulò, S., Porzi, L., Kotschieder, P.: Revising densification in gaussian splatting. In: ECCV (2024) [9](#)
14. Cai, W., Li, X., Liu, L.: A phase shift deep neural network for high frequency approximation and wave problems. *SIAM Journal on Scientific Computing* (2020) [4](#)
15. Canny, J.: A computational approach to edge detection. TPAMI (1986) [9](#)
16. Chao, B., Tseng, H., Porzi, L., Gao, C., Li, T., Li, Q., Saraf, A., Huang, J., Kopf, J., Wetzstein, G., Kim, C.: Textured gaussians for enhanced 3D scene appearance modeling. In: CVPR (2025) [9](#), [10](#)
17. Charatan, D., Li, S., Tagliasacchi, A., Sitzmann, V.: PixelSplat: 3D gaussian splats from image pairs for scalable generalizable 3D reconstruction. In: CVPR (2024) [3](#)
18. Chen, Y., Liu, S., Wang, X.: Learning continuous image representation with local implicit image function. In: CVPR (2021) [4](#)
19. Chen, Y., Tai, Y., Liu, X., Shen, C., Yang, J.: FSRNet: End-to-end learning face super-resolution with facial priors. In: CVPR (2018) [14](#)
20. Chen, Z., Funkhouser, T., Hedman, P., Tagliasacchi, A.: MobileNeRF: Exploiting the polygon rasterization pipeline for efficient neural field rendering on mobile architectures. In: CVPR (2023) [33](#)

21. Cohen, T., Welling, M.: Group equivariant convolutional networks. In: ICML (2016) [2](#)
22. Du, S., Wang, Y., Zhai, X., Balakrishnan, S., Salakhutdinov, R., Singh, A.: How many samples are needed to estimate a convolutional neural network? In: NeurIPS (2018) [4](#)
23. Feng, H., Aldana, D., Novello, T., De Floriani, L.: SASNet: Spatially-adaptive sinusoidal neural networks. arXiv preprint arXiv:2503.09750 (2025) [9](#)
24. Gao, R., Holynski, A., Henzler, P., Brussee, A., Martin Brualla, R., Srinivasan, P., Barron, J., Poole, B.: CAT3D: Create anything in 3D with multi-view diffusion models. In: NeurIPS (2024) [1](#), [3](#), [13](#)
25. Grossberg, M., Nayar, S.: A general imaging model and a method for finding its parameters. In: ICCV (2001) [13](#)
26. Guizilini, V., Irshad, M., Chen, D., Shakhnarovich, G., Ambrus, R.: Zero-shot novel view and depth synthesis with multi-view geometric diffusion. In: CVPR (2025) [3](#)
27. Hamdi, A., Melas-Kyriazi, L., Mai, J., Qian, G., Liu, R., Vondrick, C., Ghanem, B., Vedaldi, A.: GES: Generalized exponential splatting for efficient radiance field rendering. In: CVPR (2024) [9](#)
28. Hedman, P., Philip, J., Price, T., Frahm, J., Drettakis, G., Brostow, G.: Deep blending for free-viewpoint image-based rendering. SIGGRAPH (2018) [8](#), [9](#), [27](#), [28](#), [35](#)
29. Held, J., Vandeghen, R., Hamdi, A., Deliege, A., Cioppa, A., Giancola, S., Vedaldi, A., Ghanem, B., Van Droogenbroeck, M.: 3D convex splatting: Radiance field rendering with 3D smooth convexes. In: CVPR (2025) [9](#)
30. Hu, J., Song, B., Xu, X., Shen, L., Fessler, J.: Learning image priors through patch-based diffusion models for solving inverse problems. In: NeurIPS (2024) [3](#)
31. Huang, L., Bai, J., Guo, J., Li, Y., Guo, Y.: On the error analysis of 3D gaussian splatting and an optimal projection strategy. In: ECCV (2024) [3](#), [9](#)
32. Huang, Z., Wu, C., Guo, Y., Huang, X., Ren, L.: 3DGEER: 3D gaussian rendering made exact and efficient for generic cameras. In: ICLR (2026) [9](#)
33. Huh, M., Mobahi, H., Zhang, R., Cheung, B., Agrawal, P., Isola, P.: The low-rank simplicity bias in deep networks. TMLR (2022) [3](#)
34. Jin, H., Jiang, H., Tan, H., Zhang, K., Bi, S., Zhang, T., Luan, F., Snavely, N., Xu, Z.: LVSM: A large view synthesis model with minimal 3D inductive bias. In: ICLR (2025) [3](#)
35. Karras, T., Aila, T., Laine, S., Lehtinen, J.: Progressive growing of GANs for improved quality, stability, and variation. In: ICLR (2018) [2](#), [30](#)
36. Karras, T., Laine, S., Aila, T.: A style-based generator architecture for generative adversarial networks. In: CVPR (2019) [30](#)
37. Keil, S., Yu, A., Tancik, M., Chen, Q., Recht, B., Kanazawa, A.: Plenoxels: Radiance fields without neural networks. In: CVPR (2022) [9](#)
38. Kerbl, B., Kopanas, G., Leimkühler, T., Drettakis, G.: 3D gaussian splatting for real-time radiance field rendering. SIGGRAPH (2023) [1](#), [2](#), [4](#), [5](#), [9](#), [10](#), [11](#), [12](#), [21](#), [27](#), [30](#), [32](#), [33](#), [34](#), [35](#), [36](#), [37](#)
39. Kheradmand, S., Rebain, D., Sharma, G., Sun, W., Tseng, Y., Isack, H., Kar, A., Tagliasacchi, A., Yi, K.: 3D gaussian splatting as markov chain monte carlo. In: NeurIPS (2024) [2](#), [3](#), [9](#), [10](#), [12](#), [21](#), [27](#), [32](#), [34](#), [35](#), [36](#), [37](#)
40. Knapitsch, A., Park, J., Zhou, Q., Koltun, V.: Tank & Temples: Benchmarking large-scale scene reconstruction. SIGGRAPH (2017) [8](#), [9](#), [27](#), [28](#)

41. Lahoti, A., Karp, S., Winston, E., Singh, A., Li, Y.: Role of locality and weight sharing in image-based tasks: A sample complexity separation between CNNs, LCNs, and FCNs. In: ICLR (2024) 4
42. LeCun, Y., Bottou, L., Bengio, Y., Haffner, P.: Gradient-based learning applied to document recognition. *Proceedings of the IEEE* (1998) 2
43. Lee, J., Jin, K.H.: Local texture estimator for implicit representation function. In: CVPR (2022) 4
44. Lee, J., Kim, W., Gwak, D., Choi, E.: Conditional generation of periodic signals with fourier-based decoder. In: *NeurIPS Workshop on Deep Generative Models and Downstream Applications* (2021) 2, 4
45. Lenc, K., Vedaldi, A.: Understanding image representations by measuring their equivariance and equivalence. In: CVPR (2015) 4
46. Li, H., Liu, J., Sznajder, M., Camps, O.: 3D-HGS: 3D half-gaussian splatting. In: CVPR (2025) 2, 3, 9
47. Li, R., Yi, B., Liu, J., Gao, H., Ma, Y., Kanazawa, A.: Cameras as relative positional encoding. In: *NeurIPS* (2025) 3
48. Li, Z., Zhang, Y., Arora, S.: Why are convolutional nets more sample-efficient than fully-connected nets? In: ICLR (2021) 4
49. Liu, R., Lehman, J., Molino, P., Petroski Such, F., Frank, E., Sergeev, A., Yosinski, J.: An intriguing failing of convolutional neural networks and the coordconv solution. In: *NeurIPS* (2018) 2, 6, 37, 38
50. Liu, Z., Zhu, H., Zhang, Q., Fu, J., Deng, W., Ma, Z., Guo, Y., Cao, X.: FINER: Flexible spectral-bias tuning in implicit neural representation by variable-periodic activation functions. In: CVPR (2024) 4, 10, 12, 13
51. Llocoz, N., Mirzaei, A., Perel, O., Lutio, R., Esturo, J., State, G., Fidler, S., Sharp, N., Gojcic, Z.: 3D gaussian ray tracing: Fast tracing of particle scenes. *SIGGRAPH* (2024) 3, 9
52. Lu, C., Yin, F., Chen, X., Liu, W., Chen, T., Yu, G., Fan, J.: A large-scale outdoor multi-modal dataset and benchmark for novel view synthesis and implicit scene reconstruction. In: ICCV (2023) 8, 9, 27, 28, 35
53. Mai, A., Hedman, P., Kopanas, G., Verbin, D., Futschik, D., Xu, Q., Kuester, F., Barron, J., Zhang, Y.: EVER: Exact volumetric ellipsoid rendering for real-time view synthesis. In: ICCV (2025) 9, 32
54. Maiorov, V., Meir, R.: Lower bounds for multivariate approximation by affine-invariant dictionaries. *IEEE Transactions on Information Theory* (2002) 24
55. Malach, E., Shalev-Shwartz, S.: Computational separation between convolutional and fully-connected networks. In: ICLR (2021) 4
56. Malarz, D., Smolak-Dyżewska, W., Tabor, J., Tadeja, S., Spurek, P.: Gaussian splatting with NeRF-based color and opacity. *CVIU* (2025) 9, 32
57. Mei, S., Misiakiewicz, T., Montanari, A.: Learning with invariances in random features and kernel models. In: *CoLT* (2021) 4
58. Menon, S., Damian, A., Hu, S., Ravi, N., Rudin, C.: Pulse: Self-supervised photo upsampling via latent space exploration of generative models. In: CVPR (2020) 14
59. Mildenhall, B., Srinivasan, P., Tancik, M., Barron, J., Ramamoorthi, R., Ng, R.: NeRF: Representing scenes as neural radiance fields for view synthesis. In: *ECCV* (2020) 2, 3, 5, 8, 9, 10, 12, 13, 14, 27, 28, 35
60. Misiakiewicz, T., Mei, S.: Learning with convolution and pooling operations in kernel methods. In: *NeurIPS* (2022) 4

61. Müller, T., Evans, A., Schied, C., Keller, A.: Instant neural graphics primitives with a multiresolution hash encoding. SIGGRAPH (2022) [3](#), [4](#), [5](#), [9](#), [10](#), [14](#), [30](#), [33](#), [37](#)
62. Park, J., Florence, P., Straub, J., Newcombe, R., Lovegrove, S.: DeepSDF: Learning continuous signed distance functions for shape representation. In: CVPR (2019) [14](#)
63. Paszke, A., Gross, S., Massa, F., Lerer, A., Bradbury, J., Chanan, G., Killeen, T., Lin, Z., Gimelshein, N., Antiga, L., Desmaison, A., Kopf, A., Yang, E., DeVito, Z., Raison, M., Tejani, A., Chilamkurthy, S., Steiner, B., Fang, L., Bai, J., Chintala, S.: PyTorch: An imperative style, high-performance deep learning library. In: NeurIPS (2019) [28](#)
64. Pogodin, R., Mehta, Y., Lillicrap, T., Latham, P.: Towards biologically plausible convolutional networks. In: NeurIPS (2021) [4](#)
65. Rahaman, N., Baratin, A., Arpit, D., Draxler, F., Lin, M., Hamprecht, F., Bengio, Y., Courville, A.: On the spectral bias of neural networks. In: ICML (2019) [3](#)
66. Rahimi, A., Recht, B.: Random features for large-scale kernel machines. In: NeurIPS (2007) [4](#)
67. Rematas, K., Liu, A., Srinivasan, P., Barron, J., Tagliasacchi, A., Funkhouser, T., Ferrari, V.: Urban radiance fields. In: CVPR (2022) [33](#), [34](#)
68. Saharia, C., Ho, J., Chan, W., Salimans, T., Fleet, D., Norouzi, M.: Image super-resolution via iterative refinement. TPAMI (2022) [4](#), [14](#), [30](#), [31](#)
69. Saratchandran, H., Ramasinghe, S., Lucey, S.: From activation to initialization: Scaling insights for optimizing neural fields. In: CVPR (2024) [4](#), [10](#), [12](#), [13](#)
70. Sawada, N., Miraldo, P., Lohit, S., Marks, T., Chatterjee, M.: FreBIS: Frequency-based stratification for neural implicit surface representations. In: CVPR Workshops (2025) [4](#)
71. Schnepf, A., Kassab, K., Franceschi, J., Caraffa, L., Vasile, F., Mary, J., Comport, A., Gouet-Brunet, V.: Bringing NeRFs to the latent space: Inverse graphics autoencoder. In: ICLR (2025) [3](#)
72. Sharma, G., Rebain, D., Tagliasacchi, A., Yi, K.: Volumetric rendering with baked quadrature fields. In: ECCV (2024) [9](#), [27](#), [28](#)
73. Sitzmann, V., Martel, J., Bergman, A., Lindell, D., Wetzstein, G.: Implicit neural representations with periodic activation functions. In: NeurIPS (2020) [2](#), [4](#), [10](#)
74. Stanley, K.: Compositional pattern producing networks: A novel abstraction of development. Genetic programming and evolvable machines (2007) [5](#)
75. Sun, W., Trulls, E., Tseng, Y., Sambandam, S., Sharma, G., Tagliasacchi, A., Yi, K.: PointNeRF++: a multi-scale, point-based neural radiance field. In: ECCV (2024) [34](#)
76. Talegaonkar, C., Belhe, Y., Ramamoorthi, R., Antipa, N.: Volumetrically consistent 3D gaussian rasterization. In: CVPR (2025) [9](#)
77. Tancik, M., Srinivasan, P., Mildenhall, B., Fridovich-Keil, S., Raghavan, N., Singhal, U., Ramamoorthi, R., Barron, J., Ng, R.: Fourier features let networks learn high frequency functions in low dimensional domains. In: NeurIPS (2020) [2](#), [3](#), [4](#), [5](#), [10](#), [12](#), [13](#), [14](#), [29](#), [30](#)
78. Tancik, M., Weber, E., Ng, E., Li, R., Yi, B., Wang, T., Kristoffersen, A., Austin, J., Salahi, K., Ahuja, A., Mcallister, D., Kerr, J., Kanazawa, A.: Nerfstudio: A modular framework for neural radiance field development. In: SIGGRAPH (2023) [28](#)
79. Tang, J., Ren, J., Zhou, H., Liu, Z., Zeng, G.: DreamGaussian: Generative gaussian splatting for efficient 3D content creation. In: ICLR (2024) [1](#)

80. Teney, D., Nicolicioiu, A., Hartmann, V., Abbasnejad, E.: Neural redshift: Random networks are not random functions. In: CVPR (2024) [4](#)
81. Timofte, R., Agustsson, E., Van Gool, L., Yang, M., Zhang, L.: NTIRE 2017 challenge on single image super-resolution: Methods and results. In: CVPR workshops (2017) [30](#), [31](#)
82. Ulyanov, D., Vedaldi, A., Lempitsky, V.: Deep image prior. In: CVPR (2018) [4](#)
83. Vaswani, A., Shazeer, N., Parmar, N., Uszkoreit, J., Jones, L., Gomez, A., Kaiser, Ł., Polosukhin, I.: Attention is all you need. In: NeurIPS (2017) [4](#)
84. Wang, L., Ren, Q., Liao, K., Wang, H., Chen, Z., Tang, Y.: StableGS: A floater-free framework for 3D gaussian splatting. arXiv preprint arXiv:2503.18458 (2025) [2](#), [3](#), [9](#)
85. Wang, X., Xie, L., Dong, C., Shan, Y.: Real-ESRGAN: Training real-world blind super-resolution with pure synthetic data. In: ICCV (2021) [4](#), [14](#), [21](#), [30](#), [31](#)
86. Wang, X., Yu, K., Dong, C., Loy, C.: Recovering realistic texture in image super-resolution by deep spatial feature transform. In: CVPR (2018) [30](#), [31](#)
87. Wang, Y., Lai, C.: Multi-stage neural networks: Function approximator of machine precision. Journal of Computational Physics (2024) [4](#)
88. Wang, Z., Bovik, A., Sheikh, H., Simoncelli, E.: Image quality assessment: from error visibility to structural similarity. TIP (2004) [9](#), [27](#), [30](#), [31](#)
89. Wang, Z., Shen, T., Nimier-David, M., Sharp, N., Gao, J., Keller, A., Fidler, S., Müller, T., Gojcic, Z.: Adaptive shells for efficient neural radiance field rendering. SIGGRAPH (2023) [8](#), [9](#), [27](#), [28](#), [35](#)
90. Wang, Z., Wu, L.: Theoretical analysis of the inductive biases in deep convolutional networks. In: NeurIPS (2023) [4](#)
91. Wang, Z., Xu, D.: HyRF: Hybrid radiance fields for efficient and high-quality novel view synthesis. In: NeurIPS (2025) [9](#)
92. Wu, Q., Esturo, J., Mirzaei, A., Moenne-Loccoz, N., Gojcic, Z.: 3DGUT: Enabling distorted cameras and secondary rays in gaussian splatting. In: CVPR (2025) [9](#)
93. Xu, A., Raginsky, M.: Minimum excess risk in bayesian learning. IEEE Transactions on Information Theory (2022) [23](#)
94. Yang, G., Salman, H.: A fine-grained spectral perspective on neural networks. arXiv preprint arXiv:1907.10599 (2019) [4](#), [10](#), [12](#), [13](#)
95. Ye, V., Li, R., Kerr, J., Turkulainen, M., Yi, B., Pan, Z., Seiskari, O., Ye, J., Hu, J., Tancik, M., Kanazawa, A.: gsplat: An open-source library for Gaussian splatting. arXiv preprint arXiv:2409.06765 (2024) [28](#)
96. Yu, L., Li, Z., Xiao, J., Gabbouj, M.: High-frequency enhanced hybrid neural representation for video compression. Expert Systems with Applications (2025) [4](#)
97. Yu, Z., Chen, A., Huang, B., Sattler, T., Geiger, A.: Mip-Splatting: Alias-free 3D gaussian splatting. In: CVPR (2024) [2](#), [3](#), [9](#), [27](#), [36](#), [37](#)
98. Yuan, Y., Li, X., Huang, Y., De Mello, S., Nagano, K., Kautz, J., Iqbal, U.: GAavatar: Animatable 3D gaussian avatars with implicit mesh learning. In: CVPR (2024) [1](#)
99. Yue, Z., Wang, J., Loy, C.: ResShift: Efficient diffusion model for image super-resolution by residual shifting. In: NeurIPS (2023) [4](#)
100. Zhang, J., Zhan, F., Xu, M., Lu, S., Xing, E.: FreGS: 3D gaussian splatting with progressive frequency regularization. In: CVPR (2024) [2](#), [3](#), [4](#), [9](#)
101. Zhang, R., Isola, P., Efros, A., Shechtman, E., Wang, O.: The unreasonable effectiveness of deep features as a perceptual metric. In: CVPR (2018) [9](#), [27](#)
102. Zhao, J., Qiao, W., Zhang, P., Gao, H.: Quantum implicit neural representations. In: ICML (2024) [4](#)

103. Zou, Z., Yu, Z., Guo, Y., Li, Y., Liang, D., Cao, Y., Zhang, S.: Triplane meets gaussian splatting: Fast and generalizable single-view 3D reconstruction with transformers. In: CVPR (2024) [1](#)

Towards High-Fidelity Gaussian Splatting with Queried-Convolution Neural Networks

Supplementary Material

Table of Contents

A. Qualitative Results	21
A.1. 3D NVS	21
A.2. 2D Image SR	21
B. Theoretical Results	23
B.1. Benefit of Features	23
B.2. Shortcomings of Gaussian-based Representation.....	24
C. Implementation Details	27
C.1. 3D NVS	27
C.2. 1D Regression.....	29
C.3. 2D Regression.....	30
C.4. 2D Image SR	30
D. Experiments	32
D.1. 3D NVS	32
E. Supportive Explanations	37

A Qualitative Results

A.1 3D NVS

We show rendered novel-view videos from MCMC [39], MCMC + QNN, 3DGS [38] and 3DGS + QNN methods of Mip-NeRF 360 [7] scenes on the project page. We provide the red sliders to inspect details. These rendered videos show that adding QNN, faithfully renders the scene with higher fidelity compared to both the GS baselines.

A.2 2D Image SR

We provide some qualitative results of the 2D image SR experiment, with Real-ESRGAN [85] as the baseline in Fig. 7. Adding QNN to Real-ESRGAN faithfully reconstructs details in various regions and results in higher fidelity synthesis visually.

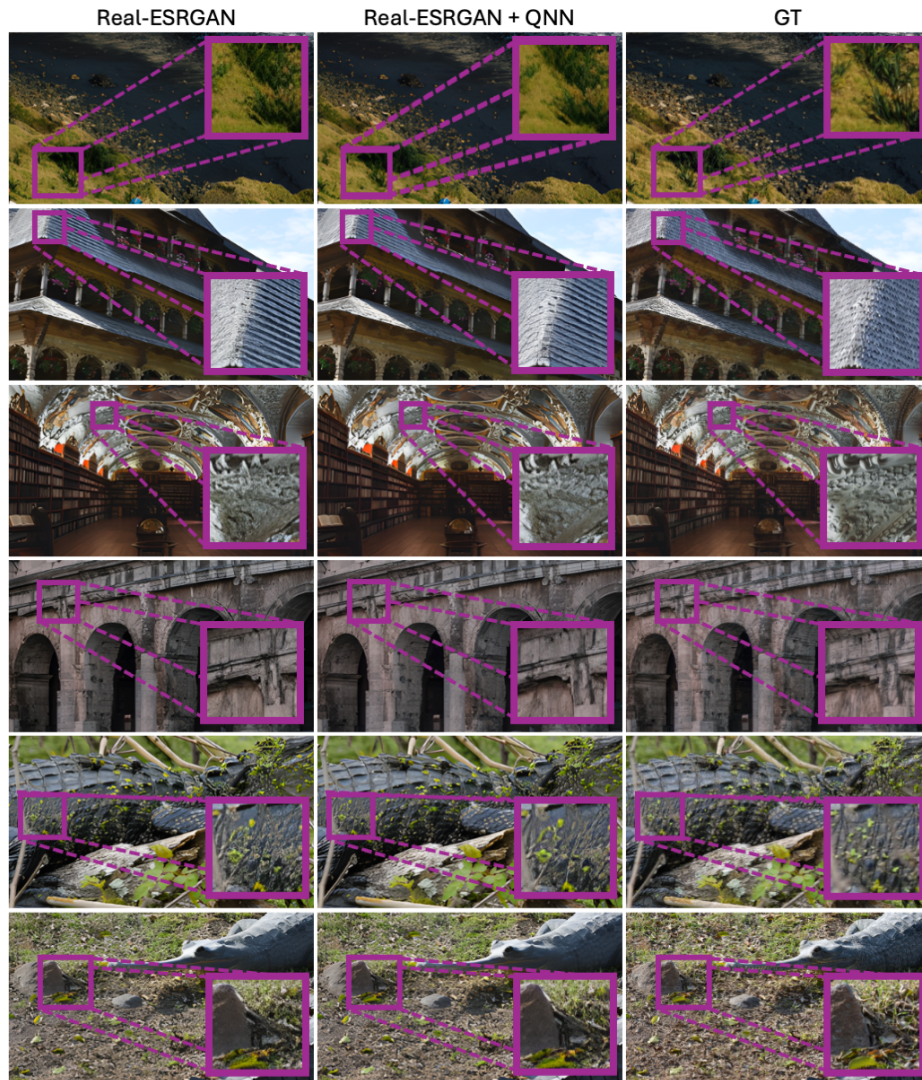


Fig. 7: SR Results of DIV2K Val images. Adding QNN to Real-ESRGAN faithfully reconstructs details in various regions and results in higher fidelity synthesis visually. We highlight the differences in inset figures.

B Theoretical Results

We next include some proofs, which we could not put in the main paper due to space constraints.

B.1 Benefit of Features

We show that adding neighborhood and queries provide the best possible risk.

Setup. The input space \mathcal{X} is either a finite discrete set or a subset of \mathbb{R}^d and $P_{\mathcal{X}}$ is a probability distribution on \mathcal{X} . The target function $f : \mathcal{X} \rightarrow [0, 1]$ is any measurable deterministic function. A feature map $\phi : \mathcal{X} \rightarrow \mathcal{Z}$ is a deterministic measurable function, mapping \mathcal{X} to a feature space \mathcal{Z} , resulting in a random variable $Z = \phi(X)$ distributed according to P_Z . The hypothesis class $\mathcal{H}(\phi)$ is the set of all deterministic measurable functions that map from \mathcal{Z} to the output space $[0, 1]$. The risk of a hypothesis $h \in \mathcal{H}(\phi)$ is the expected squared (MSE) loss: $\mathcal{R}(h, \phi, f) = \mathbb{E}_{P_X} [(f(X) - h(\phi(X)))^2]$. And the best achievable risk for a feature map ϕ is $\mathcal{R}^*(\phi, f) = \min_{h \in \mathcal{H}(\phi)} \mathcal{R}(h, \phi, f)$.

Lemma 1 (Best achievable risk). *The lowest achievable risk for a feature map ϕ is $\mathcal{R}^*(\phi, f) = \mathbb{E}_{P_Z} [\mathbb{V}_{P_{X|Z}}(f(X)|Z)]$.*

Proof. Given that we are using the squared loss, and since f is a deterministic function, the optimal predictor is given by [10, Eq. (3.36)]:

$$h^*(Z) = \mathbb{E}_{P_{X|Z}}[f(X)|Z].$$

Since f and ϕ are deterministic and measurable, the conditional expectation $\mathbb{E}_{P_{X|Z}}[f(X)|Z]$ exists, is a deterministic function of Z and is measurable in Z . Furthermore, since $f(X) \in [0, 1]$ the conditional expectation also lies in $[0, 1]$. Therefore, h^* there is a deterministic measurable function from \mathcal{Z} to $[0, 1]$, and thus belongs to $\mathcal{H}(\phi)$.

The minimal risk is therefore given by:

$$\mathcal{R}^*(\phi, f) = \mathcal{R}(h^*, \phi, f) = \mathbb{E}_{P_Z} [\mathbb{E}_{P_{X|Z}} [(f(X) - h^*(Z))^2 | Z]] = \mathbb{E}_{P_Z} [\mathbb{V}_{P_{X|Z}} [f(X) | Z]]$$

where the last step uses the definition of h^* together with the definition of conditional variance.

Lemma 2 (Feature augmentation cannot worsen the best achievable risk). *Define two feature maps ϕ_i and ϕ_j where $\phi_j(X) = (\phi_i(X), \tilde{\phi}(X))$ contains the features of ϕ_i and $\tilde{\phi}$ provides some additional features. Then:*

$$\mathcal{R}^*(\phi_i, f) \geq \mathcal{R}^*(\phi_j, f).$$

Proof. Denote the random variable $F = f(X)$ and the random variables resulting from the feature maps as $Z_i = \phi_i(X)$, $\tilde{Z} = \tilde{\phi}(X)$, $Z_j = \phi_j(X) = (Z_i, \tilde{Z})$. Therefore, there exists a function $\pi(z_i, \tilde{z}_j) = z_i$ which recovers Z_i from Z_j . Thus $F \perp Z_i | Z_j$ (conditioning on Z_j already determines Z_i , so adding Z_i provides no further information). Applying the data processing inequality for Bayes risk [93] gives:

$$\mathcal{R}^*(\phi_i, f) \geq \mathcal{R}^*(\phi_j, f).$$

Lemma 3 (Including coordinates X in the features yields zero optimal risk). *Let $Z = \phi(X) = (X, \tilde{\phi}(X))$ where $\tilde{\phi}$ is some feature map. Then*

$$\mathcal{R}^*(\phi, f) = 0$$

Proof. Using Lemma 1: $\mathcal{R}^*(\phi, f) = \mathbb{E}_{P_Z}[\mathbb{V}_{P_{X|Z}}(f(X)|Z)]$. Since Z contains X , conditioning on Z determines X exactly. As f is a deterministic function of X , we have $\mathbb{V}_{P_{X|Z}}(f(X)|Z) = 0$. Therefore:

$$\mathcal{R}^*(\phi, f) = \mathbb{E}_{P_Z}[\mathbb{V}_{P_{X|Z}}(f(X)|Z)] = \mathbb{E}_{P_Z}[0] = 0.$$

Proof of Theorem 1

Proof. The different feature maps are $\phi_1(x) = (g(x))$; $\phi_2(x) = (\phi_1(x-\Delta), \phi_1(x), \phi_1(x+\Delta))$ for a fixed $\Delta > 0$; $\phi_3(x) = (\phi_2(x), x-\Delta, x, x+\Delta)$. Applying Lemma 2 twice, first with $\phi_i = \phi_1, \phi_j = \phi_2$ and then with $\phi_i = \phi_2, \phi_j = \phi_3$ results in the non-strict inequalities:

$$\mathcal{R}^*(\phi_1, f) \geq \mathcal{R}^*(\phi_2, f) \geq \mathcal{R}^*(\phi_3, f).$$

Applying Lemma 3 for $\phi = \phi_3$ shows that $\mathcal{R}^*(\phi_3, f) = 0$. Combining these results proves the theorem:

$$\mathcal{R}^*(\phi_1, f) \geq \mathcal{R}^*(\phi_2, f) \geq \mathcal{R}^*(\phi_3, f) = 0$$

B.2 Shortcomings of Gaussian-based Representation

We next present a theoretical result on the shortcoming of the Gaussian-based representations. We will show that increasing image-fidelity (increasing PSNR or decreasing MSE) for gaussian-based representation requires exponential increase in the number of Gaussians.

Theorem 2 (Approximation Error with Wavelets, Theorem 1, [54]).

Let f be a class of measurable real-valued functions defined on a compact domain in \mathbb{R}^d , and let $Y_p^{r,d}$ denote a Sobolev space function with pseudo-dimension r for some $r > 0$. Next, consider the set of n -term ψ wavelet approximations:

$$f_n^l(\psi) = \sum_{j=1}^n c_j \psi(\mathbf{A}_j x + \mathbf{b}_j), \quad (6)$$

with the affine terms $\mathbf{A}_j \in \mathbb{R}^{l \times d}$ and $\mathbf{b}_j \in \mathbb{R}^l$. For $r > 1$ and $1 \leq p, q < \infty$ satisfying $\frac{r}{d} > \left(\frac{1}{p} - \frac{1}{q}\right)_+$ and integers $1 \leq n, d < \infty$, the approximation error in L_q norm is bounded from below by

$$L_q(Y_p^{r,d}, f_n^l(\psi)) \geq \frac{c}{(n \log n)^{r/d}}, \quad (7)$$

where c is a constant independent of n .

Corollary 1 (Number of Gaussians). *Let a 2D image be a measurable real-valued function whose first derivative exists at all points. Then, the minimum number of 2D splatted Gaussians, n , required to achieve an approximation L_2 error of ϵ is bounded below by:*

$$n \geq \exp \left[W \left(\frac{c}{\epsilon} \right)^2 \right], \quad (8)$$

where W denotes the Lambert W function and c is a constant independent of ϵ .

Corollary 1 says that the number of Gaussians n required increases exponentially as the desired error ϵ decreases.

Proof. Let ϵ_q denote the approximation error, defined by the LHS of Eq. (7) in Theorem 2. Then, we have the following inequality:

$$\epsilon_q \geq \frac{c}{(n \log n)^{r/d}}$$

To find the minimum number of Gaussians n , we rearrange the inequality to get

$$n \log n \geq \left(\frac{c}{\epsilon_q} \right)^{d/r} \quad (9)$$

To solve for number of Gaussians n , we use the Lambert W function, which is defined as the inverse function of $f(w) = we^w$. The Lambert W function is the multi-valued inverse. In our case, since the number of Gaussians n must be a positive integer, we only consider the principal branch of the function, $W_0(w)$ for $w \geq 0$. We rewrite the inequality in a form that allows us to apply this function. Consider the equality case:

$$n \log n = \left(\frac{c}{\epsilon_q} \right)^{d/r} \quad (10)$$

Let $u = \log(n)$. Then, $n = \exp(u)$. Substituting, we have:

$$\begin{aligned} \exp(u) u &= \left(\frac{c}{\epsilon_q} \right)^{d/r} \\ \implies u &= W \left(\frac{c}{\epsilon_q} \right)^{d/r} \end{aligned} \quad (11)$$

Substituting back $u = \log n$ and writing for original inequality, we have:

$$n \geq \exp \left[W \left(\frac{c}{\epsilon_q} \right)^{d/r} \right]. \quad (12)$$

For splatted 3D Gaussians in 2D, the domain dimension $d=2$ and the wavelet ψ is the gaussian wavelet. Additionally, the terms c_j , \mathbf{A}_j and \mathbf{b}_j in Eq. (6) corresponds to the opacity, projected 3D covariance and projected 3D mean respectively with $l = 2$. Also, the target image function has its first derivatives defined at all points, and so, it belongs to a Sobolev space with pseudo-dimension $r=1$. Substituting these values and choose $q = 3$, $p > 6/5$ into the above inequality gives the bound:

$$n \geq \exp \left[W \left(\frac{c}{\epsilon_3} \right)^2 \right] \quad (13)$$

Let ϵ denote the MSE. Using Jensen's inequality, the norms are related by $\epsilon_3 \leq \epsilon$. Hence, we write:

$$n \geq \exp \left[W \left(\frac{c}{\epsilon} \right)^2 \right] \quad (14)$$

Thus, the number of Gaussians n required increases exponentially for decreasing the MSE ϵ .

Table 10: Near-far Planes and Initialization details for NVS datasets.

	Mip-NeRF 360 [7], Tank & Temples [40], Deep Blending [28], OMMO [52]	Shelly [89]	Syn-NeRF [59]
Near Plane	0.01	0.00	2.00
Far Plane	10^{10}	10^{10}	6.00
Normalize Space	✓	×	×
Alpha Mask	×	✓	✓
Initialization	SfM	Random	Random
Random Initial Extent	3.00	1.50	0.50
#Gaussians for MCMC	4M	3DGS	1M

C Implementation Details

We now provide some additional implementation details.

C.1 3D NVS

Datasets. Our NVS experiments use six diverse datasets with a total of 35 scenes: Mip-NeRF 360 [7], Tank & Temples [40], Deep Blending [28], OMMO [52], Shelly [89] and Syn-NeRF (Blender) [59]. This selection includes a mix of synthetic, real, bounded indoor, and unbounded outdoor scenes to ensure a comprehensive evaluation. Specifically, we use all nine scenes from Mip-NeRF 360, the same two scenes each from Tank & Temples and Deep Blending, and all eight scenes from Syn-NeRF, consistent with the 3DGS [38]. We also test on all eight scenes from the OMMO dataset, which provides scenes with distant objects [39] and all six scenes from the Shelly dataset, known for its fuzzy surfaces and complex geometries [72].

Data Splits. We take every 8th image for test and remaining as train for Mip-NeRF 360 [7], Tank & Temples [40], Deep Blending [28] and OMMO [52] datasets, as in [7]. We use the provided train/test JSONs for the Shelly [89] and Syn-NeRF [59] datasets.

Evaluation Metrics. We use Peak Signal-to-Noise Ratio (PSNR), Structural Similarity Index Metric (SSIM) [88] and VGG-16 based normalized Learned Perceptual Image Patch Similarity (LPIPS) [101] metrics [38]. We average the scores across all scenes to report a single value for each dataset.

Data Preprocessing. For data preprocessing, we follow established practices:

- *Single-scale training and single-scale testing experiments* of Tab. 2 and elsewhere: We downsample indoor Mip-NeRF 360 scenes by a factor of two and outdoor scenes by four [38]. We downsample the OMMO scene #01 images by a factor of four as in [39], while other scenes and datasets use their original image resolutions.
- *Single-scale training and multi-scale testing experiments* of Tab. 20: we train on all Mip-NeRF 360 scenes downsampled by a factor of eight and render at successively higher resolutions ($1\times$, $2\times$, $4\times$, and $8\times$) following Mip-Splat [97].

Near-far Planes and Initialization Details. We next provide dataset configurations such as near/far plane settings as well as initialization details for the datasets in Tab. 10. The datasets are grouped based on their near-far planes

and initialization parameters. Most datasets such as Mip-NeRF 360 [7], Tank & Temples [40], Deep Blending [28] and OMMO [52] utilize the default near/far planes and are initialized using standard Structure-from-Motion (SfM) data. The Shelly [89] and Syn-NeRF [59] datasets adopt custom near and far plane settings from QFields [72] and NeRF [59] respectively, and are initialized randomly due to the absence of SfM points.

Architecture. Fig. 3 shows the architecture of combining Gaussian-Splatting with QNN to enhance image fidelity. We integrate QNN into GS as follows:

- The GS renders the initial LF signal $\hat{f}^{low}(x)$.
- The QNN concatenates the query \mathbf{q} and the LF splatted image $\hat{f}^{low}(x)$.
- The QNN passes the concatenation through a CNN to produce a residual image $QNN(\mathbf{q}, \hat{f}^{low}(x))$.
- We then add the LF splatted image \hat{f}^{low} to the residual image $QNN(\mathbf{q}, \hat{f}^{low}(x))$ and produce the final predicted novel view image $\hat{f}_\theta^{GS+QNN}(x) = \hat{f}^{low}(x) + QNN(\mathbf{q}, \hat{f}^{low}(x))$.

The final prediction formulation depends on whether the dataset includes an alpha mask for opacity. Note that the final model uses 2D coordinates as queries. So, we substitute $\mathbf{q} = x$ in the following paragraphs.

- *Dataset without an Alpha Mask:* This applies to datasets such as Mip-NeRF 360, Tank & Temples, Deep Blending and OMMO datasets. The outputs of 3DGS $\hat{f}_\theta^{GS}(x)$ and 3DGS +QNN models $\hat{f}_\theta^{GS+QNN}(x)$ are as follows:

$$\hat{f}_\theta^{GS}(x) = \hat{f}^{low}(x) \quad (15)$$

$$\hat{f}_\theta^{GS+QNN}(x) = \hat{f}^{low}(x) + QNN(x \oplus \hat{f}^{low}(x)) \quad (16)$$

$$f^{GT}(x) = f(x) \quad (17)$$

- *Dataset with an Alpha Mask:* For Shelly [89] and Syn-NeRF [59] datasets, which provide an alpha mask, we follow the Nerfstudio [78] convention where the predicted or rendered RGB is considered pre-multiplied by the predicted opacity $\hat{\alpha}$ and so we do not multiply the first term by predicted opacity $\hat{\alpha}$. We multiply the GT RGB with GT opacity α . In other words, the output of 3DGS model $\hat{f}_\theta^{GS}(x)$, 3DGS +QNN model $\hat{f}_\theta^{GS+QNN}(x)$ and the GT $f^{GT}(x)$ are as follows:

$$\hat{f}_\theta^{GS}(x) = \hat{f}^{low}(x) + (1 - \hat{\alpha}(x)) * b \quad (18)$$

$$\hat{f}_\theta^{GS+QNN}(x) = \hat{f}^{low}(x) + QNN(\hat{\alpha}(x) * [x \oplus \hat{f}^{low}(x)]) + (1 - \hat{\alpha}(x)) * b \quad (19)$$

$$f^{GT}(x) = \alpha f(x) + (1 - \alpha(x)) * b, \quad (20)$$

with b being the background color, which is set to white for all pixels.

Implementation. Our implementation uses the *gsplat* library⁵ [95] and PyTorch [63]. Traditional MLPs process coordinate queries with fully-connected layers to output a three-channel RGB residual image. In contrast, QNNs leverages 2D convolutions to process both the 2D coordinate queries and the LF splatted image, and output a three-channel RGB residual image.

⁵ <https://github.com/nerfstudio-project/gspat>

All MLPs use 4 linear layers with 256 dimensions and ReLUs. To ensure a fair comparison with MLP, we implement QNN with reduced input channels by a factor of 4. Thus, QNN uses 4 2D convolutional layers, a 3×3 kernel size, 64 channels, ReLU activations and utilizes vanilla encodings. We experiment with other encodings for QNN in the Sec. 5.3: *Encodings* paragraph.

Loss. We compare the prediction from the GS+QNN model $\hat{f}_\theta^{GS+QNN}(x)$ against the GT image $f^{GT}(x)$ with the same loss as the corresponding baseline.

Optimization. For QNN models, the QNN parameters are trained with AdamW optimizer with a learning rate of $1e-4$. We train with all architectures in an end-to-end learning framework and apply QNN after 75% of total iterations (*e.g.*: after 22,500 iterations for total of 30,000 iterations) without changing the total iterations.

C.2 1D Regression

Dataset. Our experiments use the synthetic 1D $1/f^\alpha$ signal, defined on the interval $[0, 1)$, with $\alpha = 0.5$ [77]. The authors generate this 1D signal by sampling from a standard i.i.d. Gaussian vector of length N , scaling its j th entry by $1/j^\alpha$, and then taking the real component of its inverse Fourier transform. To fully evaluate the networks’ ability to learn HF signals, we remove the signal’s bandlimitedness. We then apply a low-pass filter with a normalized cutoff of 0.125 to separate this signal into its low- and residual components, and our task is regressing only the residual component.

Data Splits. For training and testing, we randomly sample data points, using a signal length $N=32$ [77].

Evaluation Metrics. We use the PSNR metric for evaluation.

Baselines. We use MLP with vanilla and Fourier encodings [77] as our baselines.

Implementation. The MLP architecture consists of 4 linear layers with 256 dimensions and ReLUs [77] to output 1D signal. The Fourier MLPs use the default setting of 256-dimensional cosines and sines each randomly sampled from the standard deviation of 10 as [77]. The MLP takes 1D queries as input, and so we replace the linear layer in MLP with 1D convolution to construct CNN and QNN. Note that the QNN takes both the 1D coordinates and LF component as inputs, while the CNN takes only LF component as input. We use QNN with Vanilla encodings. To ensure a fair comparison, we reduce the input channels of CNN and QNN architectures by a factor of $\sqrt{3}$ to match the parameter count with vanilla MLP, as they use a 1D convolution kernel size of 3. Since all these networks predict the residual signal, we add the LF component to these signal to obtain the final predicted signal, which we then use for PSNR metric calculation. Please refer to Tab. 1 for the experimental settings.

Loss. We train with the \mathcal{L}_1 loss on the training samples to avoid data leakage.

Optimization. We train all models with Adam optimizer with learning rate $1e-5$ for 500 iterations.

C.3 2D Regression

Datasets. We use the Mip-NeRF 360 dataset [7] for this experiment, and the rendered output from the baseline 3DGS [38] as the low-fidelity image input to the QNN. The QNN learns to predict the residual error left by 3DGS with respect to the GT image. Specifically, the final prediction is the sum of 3DGS-splatted image (LF baseline) plus the QNN’s predicted residual image.

Data Splits. We randomly sample training and validation pixels over images.

Evaluation Metrics. We use the PSNR and SSIM [88] metrics for evaluation as [77] over both validation and training pixels. We run over all scenes of the Mip-NeRF 360 dataset [7] and average scores across scenes to report a single value for each model.

Baselines. We use the MLP with vanilla encodings, Fourier encodings [77] and hash-grids [61] as our baselines.

Implementation. The MLP architecture has 4 linear layers, 256 dimensions and ReLUs to output three-dimensional RGB signal. The Fourier MLPs use the default setting of 256-dimensional cosines and sines each randomly sampled from the standard deviation of 10 as [77]. The MLPs take 2D coordinate queries as input, and so, we replace the linear layer in MLP with 2D convolution and append LF image to construct QNN. We use QNN with both Vanilla and Fourier encodings. To ensure a fair comparison, we reduce the input channels of QNN architectures by a factor of 3 to match the parameter count with vanilla MLP, as QNN uses a 2D convolution kernel size of 3×3 . Since all these networks predict the residual output, we add the LF component to these outputs to obtain the final predicted outputs, which we then use for metric calculation. Please refer to Tab. 1 for the experimental settings.

Loss. We calculate the \mathcal{L}_1 loss between the final prediction and the GT Mip-NeRF 360 image. Note that we calculate the \mathcal{L}_1 loss on the training samples to avoid data leakage.

Optimization. We train all models with Adam optimizer with learning rate $1e-3$ for 2,000 iterations as [77].

C.4 2D Image SR

Our experimental setup encompasses two distinct image SR scenarios:

- Face SR: This sub-task involves $8 \times$ upscaling of face images from 16×16 to 128×128 resolution.
- Natural SR: This sub-task involves $4 \times$ upscaling of natural images from 64×64 to 256×256 [85].

Datasets. The face SR experiments use Flickr-Faces-HQ dataset [36] for training and CelebA-HQ for evaluation as [68]. The natural SR experiments use DIV2K [2], Flickr2K [81] and OST [86] datasets for training and DIV2K validation images for evaluation following [85].

Data Splits. For face SR, we leverage the FFHQ dataset [36], utilizing all its 70,000 images for training, and test on 30,000 CelebA-HQ dataset [35] as in [68]. For natural SR, our training follows Real-ESRGAN [85], comprising 13,774 HR

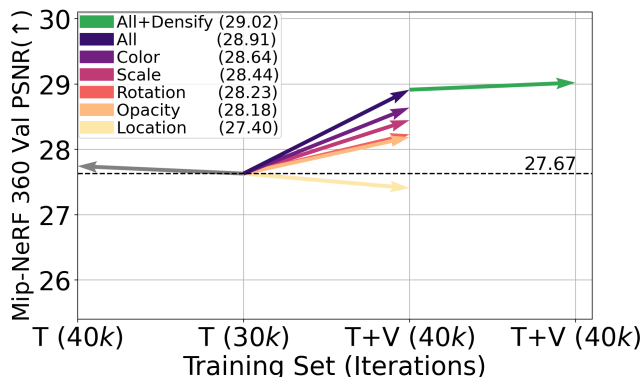


Fig. 8: Oracle Analysis on the Mip-NeRF 360 dataset [7] finetuning one or all of the gaussian primitive parameters with validation PSNR in parentheses. **Color (SH) parameters are the most important parameter** for improving visual fidelity. The figure shows that extra training time [T(30k)→T(40k)] does not significantly change the validation PSNR, while densification (All+Densify) also does not help if we have finetuned all parameters (All) on the validation images.

images, with 800 train images from DIV2K [2], 2,650 images from Flickr2K [81] and 10,324 images from the OST dataset [86]. We evaluate on the paired 100 DIV2K validation images.

Evaluation Metrics. We use the widely accepted PSNR and SSIM [88] metrics [68] for evaluation.

Baselines. To thoroughly assess the impact of our proposed QNN, we integrate it into two prominent architectural paradigms: diffusion models and GANs. We use SR3 [68], a DDPM-based SR method and Real-ESRGAN [85], a GAN-based SR method as our baselines.

Implementation. For face SR, we use an unofficial implementation⁶ of SR3 [68], a DDPM-based SR method. For natural SR, we leverage the official Real-ESRGAN [85] codebase⁷. We integrate QNN into both SR3 [68] and Real-ESRGAN [85] methods. It is crucial to note that both the original SR3 and Real-ESRGAN models use CNN architectures and take the LR input. We realise QNN by augmenting these existing CNN models with 2D coordinate queries. Note that QNN has slightly more number of parameters (0.0068% more for Real-ESRGAN generator) than CNN because input to the QNN is a 5-channel image (3 RGB + 2 coordinates) compared to 3-channel RGB image as input to the CNN. For the SR experiments, we directly predict the desired signal without adding the LF signal since the backbones contain residual connections.

Loss and Optimization. We train the CNN baseline and QNN-augmented models with exactly same loss functions, iterations and other hyper-parameters.

⁶ <https://github.com/Janspiry/Image-Super-Resolution-via-Iterative-Refinement> SR3 does not release its official code. We do not report SR3’s natural SR performance since this unofficial code does not reproduce natural SR results.

⁷ <https://github.com/xinntao/Real-ESRGAN>

Table 11: Mip-NeRF 360 Performance. MCMC+QNN provides Zip-NeRF-level fidelity with $10\times$ lower training and $40\times$ higher FPS than Zip-NeRF [8]. “GPU-hr” indicates the number of GPU hours it takes to train a model. “Mem.” indicates the amount of memory the finished model consumes on disk. [Key: **Best**, **Second-best**, **Third-best**, [†]= Taken from Tab. 1 of EVER [53]].

Method	PSNR (↑)	GPU-hr (↓)	FPS (↑)	Mem. (MB) (↓)
Zip-NeRF [8]	28.54	32.00 [†]	0.5 [†]	903 [†]
3DGS [38]	27.67	0.67	148.7	736
3DGS + QNN	27.96	0.83	24.8	736
MCMC [39]	28.26	2.00	135.3	900
MCMC + QNN	28.58	2.86	24.7	901

Table 12: Compute Overhead of QNN. QNN’s parameter overhead is negligible when contrasted with the standard GS parameters. [Key: MatMuls= Matrix Multiplications].

Layer	In Tensor	Out Tensor	Weight Parameters	Biases	MatMuls
1	$(C_{in}+C_{low})\times H\times W$	$C_h\times H\times W$	$(C_{in}+C_{low})\times C_h\times k\times k$	C_h	$(C_{in}+C_{low})\times C_h\times H\times W$
2 to $L-1$	$C_h\times H\times W$	$C_h\times H\times W$	$C_h\times C_h\times k\times k$	C_h	$C_h\times C_h\times H\times W$
L	$C_h\times H\times W$	$C_{out}\times H\times W$	$C_{out}\times C_h\times k\times k$	C_{out}	$C_{out}\times C_h\times H\times W$
Total	–	–	$[C_{in}+C_{low}+(L-2)C_h + C_{out}]\times C_h\times k\times k$	$(L-2)C_h + C_{out}$	$[C_{in}+C_{low}+(L-2)C_h + C_{out}]\times C_h\times H\times W$

D Experiments

We next provide additional details and results of the experiments evaluating QNN’s performance.

D.1 3D NVS

Oracle Analysis of Gaussian Splatting. To determine which parameters are most critical to the performance of 3DGS [38], we conduct an “oracle analysis” using all nine scenes of the Mip-NeRF 360 dataset [7]. The 3DGS method represents a scene with a collection of 3D gaussian primitives, each defined by parameters for its location, rotation, scale, opacity, and color (represented by spherical harmonics or SH). This analysis aims to reveal which parameters contribute most significantly to the PSNR performance. The standard training procedure involves training the gaussian representation on a set of training images (T) for $30k$ iterations. In our oracle study, we extend this by taking the resulting model and finetuning it for an additional $10k$ iterations on the combined training and validation (T+V) images. To isolate the impact of each component, we finetune either a single parameter (e.g., only color) or all of them simultaneously. The results, presented in Fig. 8, show that the color (SH) parameters are the most important parameter for improving the 3DGS model’s visual fidelity. This is why predicting colors in GS+QNN model (Fig. 3) improves the PSNR on the Mip-NeRF 360 dataset [7], while predicting opacity in VDGS [56] does not improve the PSNR significantly.

Mip-NeRF 360 Performance. Tab. 11 shows the performance comparison of competing methods on Mip-NeRF 360 dataset [7]. 3DGS, 3DGS + QNN,

Table 13: Residual model ablation of the 3DGS baseline [38] on the Mip-NeRF 360 dataset. **QNN model with adding residuals performs the best.** [Key: **Best**, **Second-best**, **Third-best**].

Method	Residual	Val			Train		
		PSNR (↑)	SSIM (↑)	LPIPS (↓)	PSNR (↑)	SSIM (↑)	LPIPS (↓)
3DGS [38]	–	27.67	0.82	0.20	29.71	0.90	0.16
3DGS + QNN	None	27.40	0.82	0.20	29.32	0.90	0.16
3DGS + QNN	Multiply	27.58	0.82	0.20	29.56	0.90	0.16
3DGS + QNN	Add	27.96	0.83	0.20	30.11	0.90	0.16

Table 14: Comparison of adding sky model and adding QNN to the 3DGS baseline [38] on the Mip-NeRF 360 dataset. **Adding QNN outperforms MLP-based sky models.** [Key: **Best**, **Second-best**, **Third-best**].

Method	Val			Train		
	PSNR (↑)	SSIM (↑)	LPIPS (↓)	PSNR (↑)	SSIM (↑)	LPIPS (↓)
3DGS [38]	27.67	0.82	0.20	29.71	0.90	0.16
3DGS + Vanilla Sky [67]	27.63	0.82	0.20	29.67	0.89	0.16
3DGS + Fourier Sky	27.69	0.82	0.20	29.67	0.90	0.16
3DGS + QNN	27.96	0.83	0.20	30.11	0.90	0.16

MCMC, MCMC + QNN and Zip-NeRF models take 0.67, 0.83, 2.00, 2.86 and 32.00 GPU-hours respectively for training on a Mip-NeRF 360 scene measured with V100 GPUs. Adding QNN on top of GS baseline make the model slower in training and inference than the corresponding GS baseline. However, most importantly, MCMC + QNN provides Zip-NeRF-level fidelity with $10\times$ lower training and $40\times$ higher FPS than Zip-NeRF [8]. This is expected because QNN requires exactly one query per pixel while NeRFs require multiple queries for rendering a pixel. Existing techniques like quantized fine-tuning [20] of QNN and fusing CNN [61] could be used to speed up the QNN model further. We leave these optimizations for a future work.

Compute Overhead of QNN. We next report the computational overhead associated with integrating a QNN consisting of L layers onto a LF image of size $H \times W$ in Tab. 12. In this formulation, C_{in} , C_{low} , and C_{out} represent the query dimensions, the channels of the LF input, and the channels of the predicted image, respectively. The QNN’s architecture is further defined by the number of hidden channels C_h and the kernel size k . For the NVS task, the QNN has the following parameters:

- Layers: $L=4$.
- Channels: $C_{in}=2$, $C_{low}=3$, and $C_{out}=3$.
- Architecture: $C_h=64$ and $k=3$.

Substituting these values into the expressions in Tab. 12, the QNN introduces approximately 0.3 MB of weight and bias parameters. This parameter overhead is negligible when contrasted with the standard GS parameters, which typically exceed 700 MB. This small increase explains the Mem. numbers of Tab. 11, where including QNN results in a minimal increase in overall memory footprint.

Residual Model. QNN adds the residual signal to the LF splatted signal in Fig. 3. We next ablate this design in Tab. 13 with no residuals (None) and

Table 15: Sensitivity to initialization on baseline and QNN models on the Mip-NeRF 360 dataset. **Adding QNN outperforms** the baselines on both val and train images across initializations. [Key: Init= Initialization].

Method	Init	QNN	Val			Train		
			PSNR (↑)	SSIM (↑)	LPIPS (↓)	PSNR (↑)	SSIM (↑)	LPIPS (↓)
3DGS [38]	SfM	×	27.67	0.82	0.20	29.71	0.90	0.16
		✓	27.96 (+0.29)	0.83 (+0.01)	0.20 (+0.00)	30.11 (+0.41)	0.90 (+0.00)	0.16 (+0.00)
	Random	×	26.28	0.77	0.26	28.19	0.85	0.21
		✓	26.82 (+0.54)	0.79 (+0.02)	0.23 (+0.03)	29.85 (+1.66)	0.89 (+0.04)	0.17 (+0.04)
MCMC [39]	SfM	×	28.26	0.84	0.17	30.31	0.91	0.14
		✓	28.58 (+0.32)	0.84 (+0.00)	0.16 (+0.01)	30.69 (+0.38)	0.91 (+0.00)	0.14 (+0.00)
	Random	×	27.28	0.81	0.20	30.07	0.90	0.15
		✓	27.51 (+0.23)	0.81 (+0.00)	0.20 (+0.00)	30.38 (+0.31)	0.91 (+0.01)	0.15 (+0.00)

Table 16: Sensitivity to number of layers in QNN with 3DGS [38] on the Mip-NeRF 360 dataset. QNN uses 4 layers. We refrain from highlighting if there are more than 5 entries with the same number. [Key: Best, Second-best, Third-best].

Layers	Val			Train		
	PSNR (↑)	SSIM (↑)	LPIPS (↓)	PSNR (↑)	SSIM (↑)	LPIPS (↓)
0	27.67	0.82	0.20	29.71	0.90	0.16
2	27.81	0.82	0.20	29.85	0.90	0.16
3	27.89	0.83	0.20	30.01	0.90	0.16
4	27.96	0.83	0.20	30.11	0.90	0.16
5	27.91	0.83	0.20	30.13	0.90	0.16
6	27.90	0.83	0.20	30.12	0.90	0.16

multiplying residuals (Multiply). Tab. 13 results show that QNN model with adding the residual performs the best.

Sky Model. A related baseline is the sky model [67, 75], which is an MLP network with a sigmoid and that maps view directions to a residual color. We compare QNN with vanilla sky and Fourier encoded sky models in Tab. 14. Tab. 14 shows that QNN outperforms MLP-based sky models as well.

Sensitivity to Initialization. GS methods are sensitive to initialization [38]. We, therefore, analyze the impact of SfM and random initialization on all nine scenes of the Mip-NeRF 360 dataset [7]. We experiment with both 3DGS [38] and MCMC [39] baselines in Tab. 15. Tab. 15 results show that QNN remains effective for both these initializations for both baselines.

Sensitivity to Number of Layers. Finally, we experiment with the number of convolution layers to pinpoint the optimal QNN depth in Tab. 16. We found that reducing the number of layers below four negatively impacted performance, while increasing the count beyond four did not provide any additional benefit. Hence, QNN for NVS uses four layers.

Sensitivity to LF Signal Quality. We used the final number of Gaussians in the MCMC baseline [39] on Mip-NeRF 360 dataset [7] as a proxy for the quality of the LF signal, with lower number of gaussians representing lower fidelity signal, while higher number of gaussians representing higher fidelity signal. As shown in Fig. 4, adding QNN provides consistent PSNR improvements at varying quality of LF signal. This demonstrates the robustness of QNN, affirming its ability to work with varying LF signal quality.

Table 17: Detailed NVS Results. This is the detailed version of Tab. 2. **Adding QNN outperforms** the baselines across all datasets. Zip-NeRF Syn-NeRF numbers are from their official repository. [Key: **Best**, **Second-best**, **Third-best**, * = Retrained, T&T= Tanks and Temples, DB= Deep Blending].

Scene	Zip-NeRF [8]			3DGS* [38]			3DGS + QNN			MCMC* [39]			MCMC + QNN		
	PSNR↑ / SSIM↑ / LPIPS↓														
Mip-NeRF 360 [7]	Garden	28.20 / 0.86 / 0.12	27.67 / 0.87 / 0.10	27.88 / 0.87 / 0.10	28.00 / 0.88 / 0.10	28.25 / 0.88 / 0.09									
	Bicycle	25.80 / 0.77 / 0.21	25.60 / 0.77 / 0.20	25.68 / 0.77 / 0.20	25.97 / 0.80 / 0.17	25.99 / 0.80 / 0.16									
	Stump	27.55 / 0.80 / 0.19	26.88 / 0.78 / 0.20	27.18 / 0.79 / 0.20	27.17 / 0.80 / 0.18	27.56 / 0.81 / 0.18									
	Bonsai	34.46 / 0.95 / 0.17	32.11 / 0.95 / 0.18	32.60 / 0.95 / 0.18	33.25 / 0.96 / 0.15	33.77 / 0.96 / 0.15									
	Counter	29.38 / 0.90 / 0.19	29.10 / 0.92 / 0.18	29.28 / 0.92 / 0.18	29.86 / 0.93 / 0.15	29.98 / 0.93 / 0.15									
	Kitchen	32.50 / 0.93 / 0.12	31.39 / 0.93 / 0.11	31.80 / 0.93 / 0.11	32.30 / 0.94 / 0.10	32.81 / 0.94 / 0.10									
	Room	32.65 / 0.93 / 0.20	31.59 / 0.93 / 0.19	32.40 / 0.93 / 0.19	32.28 / 0.94 / 0.17	33.31 / 0.94 / 0.16									
	Treehill	23.89 / 0.68 / 0.27	22.81 / 0.65 / 0.31	22.75 / 0.65 / 0.31	23.27 / 0.67 / 0.27	23.34 / 0.67 / 0.27									
	Flowers	22.40 / 0.64 / 0.24	21.89 / 0.62 / 0.33	21.97 / 0.62 / 0.32	22.22 / 0.65 / 0.27	22.23 / 0.65 / 0.27									
	Average	28.54 / 0.83 / 0.19	27.67 / 0.82 / 0.20	27.96 / 0.83 / 0.20	28.26 / 0.84 / 0.17	28.58 / 0.84 / 0.16									
T&T	Truck	–	25.24 / 0.88 / 0.15	25.97 / 0.88 / 0.14	26.34 / 0.90 / 0.10	26.81 / 0.90 / 0.09									
	Train	–	21.81 / 0.81 / 0.21	22.25 / 0.81 / 0.20	22.71 / 0.85 / 0.15	22.93 / 0.85 / 0.14									
	Average	–	23.52 / 0.84 / 0.18	24.11 / 0.85 / 0.17	24.53 / 0.87 / 0.13	24.87 / 0.88 / 0.12									
DB [28]	Dr Johnson	–	29.05 / 0.90 / 0.24	29.20 / 0.90 / 0.24	29.44 / 0.91 / 0.23	29.34 / 0.91 / 0.23									
	Playroom	–	29.95 / 0.91 / 0.25	30.12 / 0.91 / 0.25	29.20 / 0.91 / 0.25	30.17 / 0.91 / 0.23									
	Average	–	29.50 / 0.90 / 0.24	29.67 / 0.91 / 0.25	29.32 / 0.91 / 0.24	29.76 / 0.91 / 0.23									
OMMO [52]	01	–	25.59 / 0.78 / 0.22	25.60 / 0.79 / 0.21	25.63 / 0.79 / 0.19	25.80 / 0.80 / 0.18									
	03	–	27.96 / 0.90 / 0.18	29.66 / 0.92 / 0.15	30.42 / 0.94 / 0.12	31.54 / 0.95 / 0.11									
	05	–	27.74 / 0.86 / 0.22	28.10 / 0.87 / 0.22	28.73 / 0.88 / 0.18	28.99 / 0.88 / 0.17									
	06	–	26.97 / 0.92 / 0.16	27.02 / 0.93 / 0.16	28.30 / 0.95 / 0.12	28.40 / 0.95 / 0.12									
	10	–	29.85 / 0.90 / 0.17	29.95 / 0.90 / 0.16	32.05 / 0.92 / 0.12	31.91 / 0.92 / 0.12									
	13	–	33.35 / 0.96 / 0.10	33.29 / 0.96 / 0.10	33.78 / 0.96 / 0.09	33.83 / 0.96 / 0.08									
	14	–	30.97 / 0.95 / 0.10	31.23 / 0.95 / 0.09	31.49 / 0.95 / 0.08	31.70 / 0.96 / 0.08									
	15	–	29.83 / 0.93 / 0.10	30.16 / 0.94 / 0.09	30.41 / 0.94 / 0.08	30.56 / 0.94 / 0.08									
	Average	–	29.03 / 0.90 / 0.16	29.37 / 0.91 / 0.15	30.10 / 0.92 / 0.12	30.34 / 0.92 / 0.12									
	Shelly [89]	Fern	–	38.69 / 0.99 / 0.03	39.10 / 0.99 / 0.02	37.55 / 0.98 / 0.03	37.67 / 0.98 / 0.03								
Horse		–	44.56 / 0.99 / 0.03	45.30 / 0.99 / 0.03	40.25 / 0.99 / 0.04	40.58 / 0.99 / 0.04									
Khady		–	32.42 / 0.90 / 0.16	32.61 / 0.90 / 0.16	33.32 / 0.91 / 0.14	33.42 / 0.91 / 0.13									
Kitten		–	39.64 / 0.98 / 0.04	40.12 / 0.98 / 0.04	39.48 / 0.98 / 0.04	39.61 / 0.98 / 0.04									
Pug		–	37.36 / 0.95 / 0.10	37.64 / 0.95 / 0.10	26.65 / 0.86 / 0.21	28.12 / 0.87 / 0.20									
Woolly		–	32.71 / 0.93 / 0.11	33.18 / 0.94 / 0.10	33.61 / 0.94 / 0.10	33.99 / 0.95 / 0.09									
Average		–	37.56 / 0.96 / 0.08	37.99 / 0.96 / 0.07	35.14 / 0.94 / 0.09	35.57 / 0.95 / 0.09									
Syn-NeRF [59]	Chair	35.78 / 0.99 / –	37.44 / 0.99 / 0.01	37.71 / 0.99 / 0.01	38.38 / 0.99 / 0.01	38.74 / 0.99 / 0.01									
	Drum	25.91 / 0.95 / –	27.71 / 0.96 / 0.03	27.84 / 0.97 / 0.03	28.10 / 0.97 / 0.03	28.23 / 0.99 / 0.03									
	Ficus	34.72 / 0.99 / –	35.49 / 0.99 / 0.01	37.66 / 0.99 / 0.01	36.54 / 0.99 / 0.01	38.08 / 0.99 / 0.01									
	Hotdog	38.05 / 0.99 / –	38.72 / 0.99 / 0.02	38.89 / 0.99 / 0.02	39.78 / 0.99 / 0.01	39.85 / 0.99 / 0.01									
	Lego	35.79 / 0.98 / –	37.63 / 0.99 / 0.01	38.05 / 0.99 / 0.01	39.26 / 0.99 / 0.01	39.39 / 0.99 / 0.01									
	Materials	31.05 / 0.97 / –	32.39 / 0.98 / 0.03	33.02 / 0.98 / 0.02	34.02 / 0.98 / 0.02	34.50 / 0.99 / 0.02									
	Mic	35.92 / 0.99 / –	36.91 / 0.99 / 0.01	37.13 / 0.99 / 0.01	39.65 / 1.00 / 0.00	40.14 / 0.99 / 0.00									
	Ship	32.33 / 0.94 / –	32.32 / 0.92 / 0.11	32.54 / 0.92 / 0.11	33.45 / 0.94 / 0.08	33.72 / 0.99 / 0.07									
	Average	33.69 / 0.97 / –	34.83 / 0.98 / 0.03	35.36 / 0.98 / 0.03	36.14 / 0.98 / 0.02	36.58 / 0.98 / 0.02									

Detailed NVS Results. We report all numbers for all scenes in Tab. 17. Tab. 17 is thus the detailed version of Tab. 2.

Variance Analysis. We next check the statistical significance of our results by running with three different seeds and reporting the mean and standard deviation on the Mip-NeRF 360 dataset [7] in Tab. 18. The table shows that integrating QNN into both the GS baselines yields statistically significant improvements.

Indoor Outdoor Analysis. We next investigate the question whether PSNR gains are statistically consistent across scenes, or dominated by a few scenes in Tab. 19. This table shows the mean PSNR across three different seeds with both 3DGS [38] and MCMC [39] baselines and their QNN-augmented models on the Mip-NeRF 360 dataset [7]. Tab. 19 confirms PSNR gains are not uniformly distributed across all scenes and larger improvements are observed specifically in indoor scenes.

Table 18: Variance Analysis on the Mip-NeRF 360 dataset. **QNN outperforming** the baselines is statistically significant. [Key: **Baseline+QNN**, **Baseline**, Avg= Average, σ = Standard Deviation].

Method	Seed	Val			Train		
		PSNR (★)	SSIM (★)	LPIPS (✦)	PSNR (★)	SSIM (★)	LPIPS (✦)
3DGS [38]	222	27.67	0.82	0.20	29.71	0.90	0.16
	111	27.65	0.82	0.20	29.69	0.90	0.16
	555	27.72	0.82	0.20	29.69	0.90	0.16
	Avg $\pm \sigma$	27.68 \pm 0.03	0.82 \pm 0.00	0.20 \pm 0.00	29.69 \pm 0.02	0.90 \pm 0.00	0.16 \pm 0.00
3DGS + QNN	222	27.96	0.83	0.20	30.11	0.90	0.16
	111	27.92	0.83	0.20	30.11	0.90	0.16
	555	27.93	0.83	0.20	30.12	0.90	0.16
	Avg $\pm \sigma$	27.92 \pm 0.03	0.83 \pm 0.00	0.20 \pm 0.00	30.12 \pm 0.02	0.90 \pm 0.00	0.16 \pm 0.00
MCMC [39]	222	28.26	0.84	0.17	30.31	0.91	0.14
	111	28.22	0.84	0.17	30.32	0.91	0.13
	555	28.31	0.84	0.17	30.31	0.91	0.13
	Avg $\pm \sigma$	28.26 \pm 0.03	0.84 \pm 0.00	0.17 \pm 0.00	30.31 \pm 0.02	0.91 \pm 0.00	0.13 \pm 0.00
MCMC + QNN	222	28.58	0.84	0.17	30.69	0.91	0.14
	111	28.53	0.84	0.17	30.67	0.91	0.14
	555	28.54	0.84	0.17	30.69	0.91	0.14
	Avg $\pm \sigma$	28.55 \pm 0.02	0.84 \pm 0.00	0.17 \pm 0.00	30.67 \pm 0.02	0.91 \pm 0.00	0.13 \pm 0.00

Table 19: Indoor-Outdoor PSNR Analysis for the NVS task on the Mip-NeRF 360 dataset averaged across three seeds. **Larger PSNR improvements are observed in indoor scenes** [Key: **Best**, **Second-best**, **Third-best**, Avg= Average].

Method	Avg	Outdoor	Indoor	Garden	Bicycle	Stump	Bonsai	Counter	Kitchen	Room	Treehill	Flowers
3DGS [38]	27.68	24.97	31.06	27.66	25.61	26.89	32.16	29.10	31.40	31.59	22.82	21.88
3DGS + QNN	27.92	25.08	31.50	27.89	25.66	27.17	32.57	29.23	31.70	32.51	22.73	21.97
MCMC [39]	28.26	25.38	31.96	28.00	25.92	27.22	33.25	29.86	32.46	32.26	23.33	22.24
MCMC + QNN	28.55	25.43	32.44	28.24	25.97	27.53	33.72	29.96	32.74	33.34	23.25	22.17

Single-scale Training and Multi-scale Testing. Contrary to most prior works that evaluate models trained on single-scale data at the same scale, we consider the new setting from Mip-Splat [97] that involves training on down-sampled resolution and testing on upsampled resolution. To simulate zoom-in effects, we train models on data downsampled by a factor of 8 and rendered at successively higher resolutions (1 \times , 2 \times , 4 \times , and 8 \times) in Tab. 20 following Mip-Splat [97]. Tab. 20 results show that adding QNN outperforms the baselines at the training scale (1 \times) and performs competitive to all SoTA methods at higher resolutions. Notably, adding QNN to the MCMC baseline again outperforms the Zip-NeRF baseline in multi-scale testing as Tab. 2 at increased resolutions, likely due to the MLPs’ inability to extrapolate to out-of-distribution details, which agrees with Tab. 2. While adding QNN performs sub-optimal to the Mip-Splat [97], these two directions are orthogonal to each other and one can add QNN to the Mip-Splat [97] as well.

Table 20: Single-scale Training and Multi-scale Testing on the Mip-NeRF 360 dataset. All methods are trained on the smallest scale (1×) and evaluated across four scales (1×, 2×, 4×, and 8×), with evaluations at higher sampling rates simulating zoom-in effects. [Key: **Best**, **Second-Best**, **Third-Best**, * = Retrained, † = Reported in Mip-Splat [97], Avg = Average].

Method	PSNR (↑)					SSIM (↑)					LPIPS (↓)					
	1×	2×	4×	8×	Avg	1×	2×	4×	8×	Avg	1×	2×	4×	8×	Avg	
Ray																
INGP† [61]	26.79	24.76	24.27	24.27	25.02	0.75	0.64	0.63	0.70	0.68	0.24	0.37	0.45	0.48	0.38	
Mip-NeRF† [7]	29.26	25.18	24.16	24.10	25.67	0.86	0.73	0.67	0.71	0.74	0.12	0.26	0.37	0.43	0.30	
Zip-NeRF† [8]	29.66	23.27	20.87	20.27	23.52	0.88	0.70	0.57	0.56	0.67	0.10	0.26	0.42	0.49	0.32	
Raster																
Mip-Splat† [97]	29.39	27.39	26.47	26.22	27.37	0.88	0.81	0.75	0.77	0.80	0.11	0.21	0.31	0.39	0.25	
3DGS* [38]	28.91	23.16	20.39	19.31	22.94	0.87	0.71	0.59	0.60	0.69	0.11	0.25	0.40	0.48	0.31	
3DGS + QNN	29.30	23.52	20.85	19.83	23.37	0.88	0.72	0.60	0.61	0.71	0.11	0.24	0.40	0.48	0.31	
MCMC (1M)* [39]	29.30	23.67	21.15	20.22	23.58	0.88	0.73	0.62	0.64	0.72	0.11	0.23	0.38	0.46	0.30	
MCMC (1M) + QNN	29.67	24.27	21.96	21.17	24.26	0.88	0.73	0.63	0.66	0.73	0.10	0.23	0.38	0.46	0.29	

E Supportive Explanations

We finally add some explanations which we could not put in the main paper because of the space constraints.

Novelty w.r.t. Coordinate CNNs. We list out the differences between Coordinate CNNs [49] and QNNs in Tab. 21. QNNs represent a generalization over Coordinate CNNs, underpinned by a distinct theoretical foundation and motivation. QNNs achieves high-fidelity results in NVS, extending the scope and impact beyond traditional Coordinate CNN applications.

Is there any regularization to keep QNN from hallucinating view-inconsistent detail across viewpoints? There is no explicit regularization to prevent the QNN from hallucinating view-inconsistent details across different viewpoints. However, our improved empirical performance on novel views suggests that added details are not inconsistent hallucinations (see next remark). Please note that the QNN model is neither generative nor pretrained elsewhere; hence, the details it adds are learned only from the given scene.

Why does adding QNN not harm 3D consistency of GS in practice?

We believe this is due to the following three reasons:

- *Residual Framework over GS:* The QNN predictions are added as a residual refinement on top of the GS output. Since GS provides a good, view-consistent starting point, QNN benefits from the consistency of the base signal.
- *Strong Multi-view Supervision:* The final output from GS + QNN model is supervised by GT multi-view images identical to the baseline GS. Hence, the model is incentivized to produce details that are at least consistent across the training views.
- *Interpolation Regime:* The NVS task operates in an interpolation regime, where test views are distributed similarly to training views. Neural networks like QNN are good at interpolation, which helps maintain consistency between views.

Table 21: Novelty w.r.t. coordinate CNNs. QNNs achieves high-fidelity results in NVS, extending the scope and impact beyond traditional Coordinate CNN applications.

	Coordinate CNN [49]	QNN
Core Claim	Spatial Coordinate Awareness	High-Fidelity Learning
Theory	×	✓
Queries	2D coordinates	1D, 2D, 3D coordinates, Raymap, Plücker or their concatenation
Tasks	ImageNet classification, MNIST detection, LSUN GAN, RL	3D NVS, 2D SR

Acknowledgements

We thank anonymous ICLR reviewers for their exceptional feedback and constructive criticism that shaped this final manuscript. We appreciate the SJC cluster admins at SRA for making our experiments possible.